The sizes, masses and specific star formation rates of massive galaxies at 1.3 <z <1.5

McLure, R. J.; Pearce, H. J.; Dunlop, J. S.; Cirasuolo, M.; Curtis-Lake, E.; Bruce, V. A.; Caputi, K. I.; Almaini, O.; Bonfield, D. G.; Bradshaw, E. J.

Published in:
Monthly Notices of the Royal Astronomical Society

DOI:
10.1093/mnras/sts092

Publication date:
2013

Monthly Notices
of the
ROYAL ASTRONOMICAL SOCIETY

MNRAS **428,** 1088–1106 (2013) doi:10.1093/mnras/sts092

The sizes, masses and specific star formation rates of massive galaxies at $1.3 < z < 1.5$: strong evidence in favour of evolution via minor mergers

R. J. McLure,[1⋆] H. J. Pearce,[1] J. S. Dunlop,[1] M. Cirasuolo,[1] E. Curtis-Lake,[1] V. A. Bruce,[1] K. I. Caputi,[1,2] O. Almaini,[3] D. G. Bonfield,[4] E. J. Bradshaw,[3] F. Buitrago,[1] R. Chuter,[3] S. Foucaud,[5] W. G. Hartley[3] and M. J. Jarvis[4]

[1]*SUPA† Institute for Astronomy, University of Edinburgh, Royal Observatory, Edinburgh EH9 3HJ*
[2]*Kapteyn Astronomical Institute, University of Groningen, PO Box 800, 9700 AV Groningen, the Netherlands*
[3]*School of Physics and Astronomy, University of Nottingham, University Park, Nottingham NG7 2RD*
[4]*Centre for Astrophysics, Science & Technology Research Institute, University of Hertfordshire, Hatfield, Herts AL10 9AB*
[5]*Department of Earth Sciences, National Taiwan Normal University, Taipei 11677, Taiwan*

Accepted 2012 September 27. Received 2012 September 18; in original form 2012 May 18

ABSTRACT

We report the results of a comprehensive study of the relationship between galaxy size, stellar mass and specific star formation rate (sSFR) at redshifts $1.3 < z < 1.5$. Based on a mass-complete ($M_\star \geq 6 \times 10^{10}\,\mathrm{M}_\odot$), spectroscopic sample from the UK Infrared Deep Sky Survey (UKIDSS) Ultradeep Survey, with accurate stellar-mass measurements derived from spectro-photometric fitting, we find that at $z \simeq 1.4$ the location of massive galaxies on the size–mass plane is determined primarily by their sSFR. At this epoch, we find that massive galaxies which are passive ($\mathrm{sSFR} \leq 0.1\,\mathrm{Gyr}^{-1}$) follow a tight size–mass relation, with half-light radii a factor of $f_\mathrm{g} = 2.4 \pm 0.2$ smaller than their local counterparts. Moreover, amongst the passive sub-sample we find no evidence that the off-set from the local size–mass relation is a function of stellar population age. In contrast, we find that massive star-forming galaxies at this epoch lie closer to the local late-type size–mass relation and are only a factor of $f_\mathrm{g} = 1.6 \pm 0.2$ smaller than observed locally. Based on a sub-sample with dynamical-mass estimates, which consists of both passive and star-forming objects, we also derive an independent estimate of $f_\mathrm{g} = 2.3 \pm 0.3$ for the typical growth in half-light radius between $z \simeq 1.4$ and the present day. Focusing on the passive sub-sample, we conclude that to produce the necessary evolution predominantly via major mergers would require an unfeasible number of merger events and overpopulate the high-mass end of the local stellar-mass function. In contrast, we find that a scenario in which mass accretion is dominated by minor mergers can comfortably produce the necessary evolution, whereby an increase in stellar mass of only a factor of $\simeq$2, accompanied by size growth of a factor of $\simeq$3.5, is required to reconcile the size–mass relation at $z \simeq 1.4$ with that observed locally. Finally, we note that a significant fraction (44 ± 12 per cent) of the passive galaxies in our sample have a disc-like morphology, providing additional evidence that separate physical processes are responsible for the quenching of star formation and morphological transformation in massive galaxies.

Key words: galaxies: evolution – galaxies: formation – galaxies: fundamental parameters – galaxies: high-redshift.

1 INTRODUCTION

Following the introduction of near-infrared (IR)-selected galaxy surveys nearly a decade ago, it became clear that a substantial population of massive, apparently evolved, galaxies was already in place by $z \simeq 1$ (e.g. Cimatti et al. 2002; Glazebrook et al. 2004), a result which was completely unexpected within the context of contemporary models of galaxy formation and evolution (e.g. Kauffmann & Haehnelt 2000). Moreover, in line with our current understanding of galaxy 'downsizing', it was quickly realized that the high-mass end of the galaxy stellar-mass function was assembled much earlier than had been expected, with studies of near-IR-selected samples

⋆E-mail: rjm@roe.ac.uk
†Scottish Universities Physics Alliance.

confirming that ≥75 per cent of the local number density of $M_\star \geq 3 \times 10^{11}\,\mathrm{M}_\odot$ galaxies was already in place by $z \simeq 1$ (e.g. Caputi et al. 2005).

Although the latest generation of galaxy evolution models are now more successful at reproducing the observed number densities of high-mass galaxies as a function of redshift (e.g. Cirasuolo et al. 2010), it has been known for several years that the physical properties of high-mass galaxies at $z \geq 1$ are substantially different from their low-redshift counterparts. Specifically, based on the *HST* imaging of near-IR-selected galaxies in the *Hubble Ultra Deep Field*, Daddi et al. (2005) noted that many high-mass ($M_\star \geq 10^{11}\,\mathrm{M}_\odot$) early-type galaxies (ETGs) at $z \geq 1.5$ displayed substantially smaller half-light radii than equivalently massive galaxies observed in the local Universe. Over the last few years, the size evolution of massive ETGs has been extensively discussed in the literature and many studies (e.g. Trujillo et al. 2007; Cimatti et al. 2008; Saracco, Longhetti & Andreon 2009; Williams et al. 2010) have reported that massive red/passive ETGs at $1 < z < 3$ are a factor of 2–5 smaller than ETGs of the same mass in the Sloan Digital Sky Survey (SDSS, Shen et al. 2003).

Despite initial concerns that results regarding the compactness of high-redshift passive galaxies could be affected by surface-brightness dimming, morphological *k*-corrections or even unresolved active galactic nuclei (AGN) components (e.g. Daddi et al. 2005), deep, high-resolution, near-IR imaging has conclusively demonstrated the compactness of many massive ($M_\star \geq 10^{11}\,\mathrm{M}_\odot$) galaxies at $z \geq 1$ (e.g. Buitrago et al. 2008; Damjanov et al. 2009). In addition, it is now well established that, within a given redshift and stellar-mass interval, early-type/passive galaxies are more compact than late-type/star-forming galaxies (e.g. Zirm et al. 2007; Toft et al. 2009; Williams et al. 2010; Wuyts et al. 2011).

In reality, the full picture is undoubtedly more complicated still, with some studies (e.g. Mancini et al. 2010) identifying examples of massive $z \geq 1$ ETGs with half-light radii fully consistent with the local size–mass relation and others (e.g. Saracco et al. 2009) finding that the population of high-redshift ETGs is comprised of a mixture of normal and compact galaxies. Moreover, it is still not currently clear whether the compact nature of some massive ETGs at high redshift is related to the age of their stellar population (Saracco et al. 2009) or not (Trujillo, Ferreras & de La Rosa 2011). Finally, there have been concerns raised in the literature that comparing massive high-redshift ETGs with the local galaxy population is subject to severe progenitor bias. For example, it has been claimed that the number densities of compact ETGs at high redshift are actually compatible with compact cluster galaxies seen locally (Valentinuzzi et al. 2010), although this has been disputed by Taylor et al. (2010). Significantly, van Dokkum et al. (2010) attempted to circumvent the progenitor bias problem by studying the size evolution of galaxies selected to have a constant number density of $n \simeq 2 \times 10^{-4}\,\mathrm{Mpc}^{-3}$ (equivalent to $M_\star \simeq 3 \times 10^{11}\,\mathrm{M}_\odot$ at $z = 0$), finding strong evidence for size evolution of the form $R_\mathrm{e} \propto (1+z)^{-1.3}$.

It is thus clear that some physical process (or processes) must be in place at high redshift which is capable of substantially increasing the half-light radii of a significant sub-set of massive high-redshift galaxies, without requiring an unphysical increase in their stellar masses. A widely advocated solution to the problem has been the 'dry-merger' scenario, whereby dense high-redshift galaxies are transformed via a series of dissipationless (i.e. dry) mergers (e.g. Cimatti, Nipoti & Cassata 2012). Such dry mergers are typically envisioned to be major mergers (i.e. mass ratio ≥ 1:3) in which the galaxy half-light radius increases in direct proportion to the accreted stellar mass. Although this scenario has several desirable characteristics, it also suffers from several obvious problems (see Nipoti et al. 2009, 2012). Principal among these is the prediction from *N*-body simulations that massive $M_\star \geq 10^{11}\,\mathrm{M}_\odot$ galaxies at $z \simeq 1.5$ are only likely to undergo one major merger over the proceeding ≃9 Gyr (e.g. Hopkins et al. 2010), strongly suggesting that major mergers *alone* cannot explain the size evolution of massive high-redshift galaxies.

An alternative mechanism invokes size growth via a sequence of minor mergers, with typical mass ratios of 1:10. The advantage of this mechanism is that in a minor merger, radius growth is expected to be proportional to the square of the accreted mass (e.g. Naab et al. 2009; Bluck et al. 2012), allowing rapid size growth without excessive growth in stellar mass. The minor-merger scenario has recently gained support from hydrodynamical simulations (e.g. Johansson, Naab & Ostriker 2012; Oser et al. 2012) and the observational results from van Dokkum et al. (2010) which demonstrate that, at a constant number density of $n \simeq 2 \times 10^{-4}\,\mathrm{Mpc}^{-3}$, the size evolution of galaxies is consistent with an 'inside-out' growth scenario. Finally, it has also been suggested (e.g. Fan et al. 2008) that feedback from AGN could expel material from the central regions of high-redshift galaxies, thereby allowing them to expand significantly at a constant stellar mass. However, the increase in stellar-velocity dispersion with redshift predicted by this model may be in conflict with the latest available data (e.g. Trujillo et al. 2011).

In this paper, we analyse the sizes, stellar masses, morphologies and specific star formation rates (sSFRs) of a unique sample of massive galaxies from the UKIDSS Ultradeep Survey (UDS) with spectroscopic redshifts in the range $1.3 < z < 1.5$. Based on this sample, we investigate the evolution in the galaxy size–mass relation over a look-back time of 9 Gyr, using accurate stellar-mass measurements derived from full spectro-photometric fitting of the available spectra and multiwavelength photometry. Armed with accurate stellar-mass measurements and star formation rates (SFRs) based on a range of empirical indicators, we investigate whether any off-set from the local size–mass scaling relations is primarily driven by morphology, stellar population age or sSFR.

The structure of this paper is as follows. In Section 2, we describe the relevant spectroscopic and photometric data, before describing the methods adopted to estimate the stellar masses and galaxy radii in Section 3. In Section 4, we present our main results on the stellar-mass–size relation and investigate the dynamical-mass–size relation for a small sub-sample of objects with reliable stellar-velocity-dispersion measurements. In Section 5, we outline a plausible evolutionary scenario which is capable of reconciling the size–mass relation of passive galaxies at $z \simeq 1.4$ with that observed locally. In Section 6, we present our final conclusions. Throughout this work, a cosmology of $H_0 = 70\,\mathrm{km\,s^{-1}\,Mpc^{-1}}$, $\Omega_\mathrm{m} = 0.3$ and $\Omega_\Lambda = 0.7$ is assumed and all magnitudes are quoted in the AB system (Oke & Gunn 1983).

2 THE DATA

All of the galaxies studied in this work have been selected from the UK Infrared Telescope (UKIRT) UDS. The UDS is the deepest of five surveys being undertaken with the UKIRT in Hawaii, which together comprise the UKIDSS (Lawrence et al. 2007). The UDS covers an area of 0.8 square degrees, is centred on $\mathrm{RA} = 02^\mathrm{h}17^\mathrm{m}48^\mathrm{s}$, $\mathrm{Dec.} = -05^\circ\,05'\,57''$ and is currently the deepest, large area, near-IR survey in existence. In addition to the available UKIRT near-IR imaging, the UDS is supported by a wide array of multiwavelength data sets, ranging from the X-ray to radio regimes (e.g. Cirasuolo et al. 2010). In this section, we briefly summarize the properties of

the UDS data sets which have been directly exploited during the course of this study.

2.1 Photometric data

The latest release of the UDS, data release eight (DR8), consists of *JHK* imaging to 5σ depths of $J = 24.9$, $H = 24.3$ and $K = 24.7$ (2 arcsec diameter apertures). Moreover, in this study we have also made use of *Y*-band imaging of the UDS ($Y = 23.6$; 5σ) obtained during the verification phase of the VISTA VIDEO survey (Jarvis et al., in press). In addition to the available near-IR imaging, the second key imaging data set in the UDS is the deep Subaru optical imaging obtained as part of the Subaru/*XMM–Newton* Deep Survey (SXDS). The SXDS imaging (Furusawa et al. 2008) covers a total area of 1.3 square degrees to 5σ depths of $B = 27.6$, $V = 27.2$, $R = 27.0$, $i' = 27.0$ and $z' = 26.0$ (2 arcsec diameter apertures). The final key data set used in this work is the Spitzer Public Legacy Survey of the UKIDSS UDS (SpUDS). The SpUDS imaging covers the full near-IR survey area and consists of IRAC imaging to 5σ depths of $3.6\mu\text{m} = 23.7$, $4.5\,\mu\text{m} = 23.3$, $5.8\,\mu\text{m} = 21.6$, $8.0\,\mu\text{m} = 21.4$ (3.8 arcsec diameter apertures) and MIPS imaging to a 5σ depth of $24\,\mu\text{m} = 18.9$ (15 arcsec diameter apertures).

2.2 Spectroscopic data

The optical spectra analysed here were observed on the VLT as part of the systematic spectroscopic follow-up of the UDS obtained through the ESO large programme ESO 180.A-0776 (UDSz; P.I. O. Almaini). Although full details of UDSz will be presented in Almaini et al. (in preparation), below we provide a brief description of the key elements within the context of this study.

The UDSz programme was allocated a total of 235 h of observations, with 93 h allocated for observations with the VIMOS spectrograph (8 pointings) and 142 h allocated for FORS2 observations (20 pointings). The primary science driver for UDSz was to obtain spectroscopic observations of a representative sample of *K*-band-selected galaxies ($K < 23$), photometrically pre-selected to lie at redshift $z_{\rm phot} \geq 1$. Consequently, the selection of primary targets was designed to obtain spectra for a random 1-in-6 sampling of $K < 23$ galaxies with $z_{\rm phot} \geq 1$ (with a control sample of $\simeq$500 galaxies with $z_{\rm phot} < 1$).

In order to exploit the different strengths of the two spectrographs, bluer galaxies ($V \leq 25$) were targeted with VIMOS and redder galaxies ($V > 25 \wedge i \leq 24.5$) were targeted with FORS2. All of the galaxies analysed in this paper were part of the spectroscopic sample observed with FORS2 and each target received 5 h of on-source integration with the medium-resolution GRS_300I grism ($6000 < \lambda < 10\,000$ Å with $R = 660$). In total, 718 ($K < 23$) galaxies were targeted with FORS2, returning 451 science-grade redshifts.

2.3 The *K*-bright galaxy sample

The sample analysed in this study consists of all 81 UDSz galaxies with robust FORS2 spectroscopic redshifts (i.e. based on multiple spectral features) in the range $1.3 \leq z \leq 1.5$ which are brighter than $K_{\rm tot} \leq 21.5$ (hereafter the *K*-bright sample). This magnitude limit is bright enough to fully exploit the large-area coverage of the UDS and to ensure that each member of the sample has an unambiguous spectroscopic redshift, while still being deep enough to produce a final sample which is mass-complete to a limit of $M_\star = 6 \times 10^{10}\,{\rm M}_\odot$, even for the most passive galaxies (see Section 4). The upper redshift limit of $z = 1.5$ was chosen to guarantee coverage of the 4000 Å break at the red end of the FORS2 spectra and the lower redshift limit of $z = 1.3$ was adopted to ensure that the FORS2 spectra also cover the age-sensitive spectral breaks at 2600 and 2800 Å.

2.3.1 A representative sample

If the results derived from this study are to be applied to the general massive galaxy population at $z \simeq 1.4$, it is clearly necessary to demonstrate that the *K*-bright sample is not a highly biased sub-set of the general galaxy population at this epoch. In order to investigate this issue, in the upper panel of Fig. 1 we plot the distribution of $i - K$ colours for the *K*-bright sample, compared to that of all $N = 1178$ galaxies in the UDS photometric redshift catalogue of Cirasuolo et al. (2010) which satisfy the criteria $1.3 \leq z_{\rm phot} \leq 1.5$ and $K_{\rm tot} \leq 21.5$. Although similar, a two-sample KS test demonstrates that the two distributions are actually statistically distinguishable at the $\geq 3\sigma$ level. As can clearly be seen from Fig. 1, unusually for a spectroscopic sample, the difference is caused by the fact that the *K*-bright sample does not feature a large enough tail of blue ($i - K < 2$) objects. This feature of the FORS2 spectroscopic sample is by design and is the result of deliberately targeting the bluer members of the UDSz sample with the VIMOS spectrograph.

In the lower panel of Fig. 1, we show the $i - K$ distribution of the *K*-bright sample compared to the $N = 970$ objects from the Cirasuolo et al. photometric redshift catalogue which satisfy $1.3 \leq z_{\rm phot} \leq 1.5$, $K_{\rm tot} \leq 21.5$ and $i - K \geq 2.2$. With this additional colour criterion the two distributions are now statistically *indistinguishable* ($p = 0.22$). For galaxies at $z \simeq 1.4$ with $K_{\rm tot} \leq 21.5$, insisting on a colour of $i - K \geq 2.2$ is effectively the same as insisting that stellar mass is $M_\star \geq 3 \times 10^{10}\,{\rm M}_\odot$ (see Section 4). Consequently, we conclude that the *K*-bright sample is a statistically random sub-sample of the galaxy population at $1.3 \leq z \leq 1.5$ with stellar masses $M_\star \geq 3 \times 10^{10}\,{\rm M}_\odot$. For information, in Table A1 of the appendix we provide the basic observational data and derived properties for the 81 members of the *K*-bright galaxy sample.

2.3.2 Sampling factor

The UDSz spectroscopic programme was designed to provide a random, 1-in-6 ($f_{\rm samp} = 6$), sampling of the $z \geq 1$ galaxy population with $K \leq 23$. However, at the $K_{\rm tot} \leq 21.5$ mag limit of the *K*-bright sample, the FORS2 component of the UDSz spectroscopy programme actually provides a significantly higher sampling rate of the very high mass end of the galaxy mass function at $1.3 < z < 1.5$. Based on the Cirasuolo et al. photometric redshift catalogue, and accounting for the differences in relative areal coverage, we calculate that, compared to the underlying galaxy population with $1.3 < z_{\rm phot} < 1.5$, $K_{\rm tot} \leq 21.5$ and $i - K \geq 2.2$, the sample factor of the *K*-bright sample is $f_{\rm samp} = 3.7 \pm 0.4$. It is this sampling factor which is adopted when comparing the *K*-bright sample to the local galaxy stellar-mass function in Section 5.

3 GALAXY MASSES, AGES AND SIZES

In addition to a precise spectroscopic redshift, for each member of the *K*-bright sample there is a deep, flux-calibrated, red-optical FORS2 spectrum and excellent multiwavelength photometry spanning the range $0.4 < \lambda < 4.5\,\mu\text{m}$. Consequently, in order to take full advantage of the available information, we have derived stellar-mass and age measurements for each member of the *K*-bright sample via

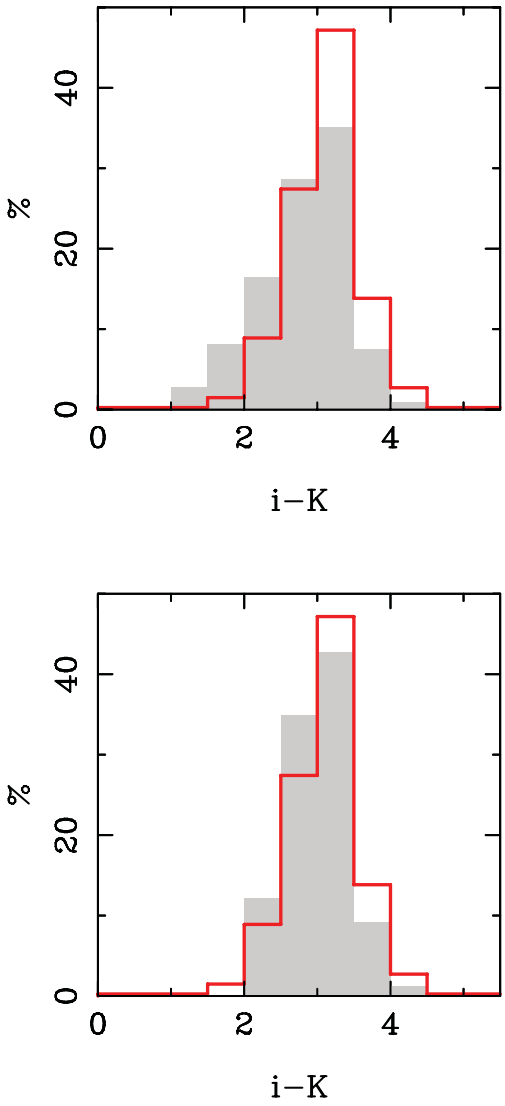

Figure 1. The top panel shows the (normalized) distribution of the $i - K$ colours of the 81 galaxies in the K-bright sample (solid red line) overplotted on the $i - K$ distribution for all $N = 1178$ galaxies in the UDS with $K_{\rm tot} \leq 21.5$ and $1.3 \leq z_{\rm phot} \leq 1.5$. The two distributions are statistically distinguishable at the $\geq 3\sigma$ level based on a two-sample KS test, which is due to the fact that, by design, the FORS2 sample does not feature the tail of blue objects with $i - K < 2$. The bottom panel compares the $i - K$ distribution of the K-bright sample to the $N = 970$ galaxies in the UDS with $K_{\rm tot} \leq 21.5$, $1.3 \leq z_{\rm phot} \leq 1.5$ and $i - K \geq 2.2$. The two distributions shown in the bottom panel are statistically *indistinguishable* ($p = 0.22$). Given the tight relationship between $i - K$ colour and stellar mass for galaxies at $z \simeq 1.4$ with $K_{\rm tot} \leq 21.5$, the bottom panel demonstrates that the K-bright sample is a random sample of the general $z \simeq 1.4$ galaxy population at stellar masses $M_\star \geq 3 \times 10^{10}\,{\rm M}_\odot$.

simultaneous spectro-photometric fitting of the FORS2 spectrum and multiwavelength photometry.

3.1 Spectro-photometric fitting

For the purposes of the spectro-photometric fitting we adopt both the Bruzual & Charlot (2003, hereafter BC03) and the Charlot & Bruzual (2007, hereafter CB07)[1] stellar population synthesis models. The CB07 models were chosen because they include an updated treatment of thermally pulsating asymptotic giant branch (TP-AGB) stars which could, at least potentially, have a large influence at rest-frame near-IR wavelengths for stellar populations with ages of $0.3 \leq t \leq 2$ Gyr (e.g. Maraston 2005). However, given that the influence of TP-AGB stars remains controversial (e.g. Kriek et al. 2010), it was decided to investigate the range of stellar masses and ages returned by both the BC03 and CB07 stellar population synthesis models.

Moreover, as galaxies are complex systems, potentially consisting of several stellar sub-systems from different generations of star formation, in some cases it is necessary to invoke models with a variety of star formation histories (SFHs) in order to obtain good fits to the data. To account for this, the data for each member of the K-bright sample was fitted using an extensive set of models encompassing a range of different SFHs, metallicities and dust attenuations.

3.1.1 *Exponentially decaying star formation rate models*

The data for each member of the K-bright sample were initially fitted using BC03 and CB07 models with exponentially decaying SFRs, the so-called τ-models. The τ-models are parametrized such that SFR $\propto \exp(-t/\tau)$, where t is the time since star formation began and τ is the e-folding time. A wide range of e-folding times were considered, with the extreme values of $\tau = 10$ and 0.1 Gyr approximating constant star formation and instantaneous burst models, respectively. As listed in Table 1, in addition to e-folding time, a wide range of ages, metallicities and dust attenuations were also explored. All models employed in the spectro-photometric fitting were based on a Chabrier (2003) initial mass function (IMF) and assumed the Calzetti et al. (2000) dust attenuation curve.

3.1.2 *DB models*

Although the τ-models effectively describe a range of different SFHs, they do not adequately describe the situation whereby the majority of a galaxy's stellar mass is produced rapidly at high redshift (and dominates rest-frame near-IR wavelengths) but a low level of more recent star formation dominates the observed flux at rest-frame ultraviolet (UV)/optical wavelengths. In order to account for this possibility, the data for each member of the K-bright sample were fitted using so-called 'double burst models' (hereafter DB models). The DB models consist of two sequential instantaneous bursts (simple stellar populations), with one component required to be 'old' (age $\geq$0.5 Gyr) and the other component required to be 'young' (age $<$ 0.5 Gyr).

The DB models were constructed by normalizing the flux of the younger stellar population to match that of the older population at a rest-frame wavelength of 5000 Å. In this way, when the components were combined, the two populations naturally accounted for different fractions of the total galaxy mass. The mass fraction of the young component was allowed to vary between 0 and 1, with a fine grid of values adopted at low-mass fractions due to the substantial impact on the rest-frame UV/optical from even small amounts of recent star formation. Finally, dust reddening was applied to the combined young+old stellar population using the Calzetti (2000)

[1] Stéphane Charlot, private communication.

Table 1. The parameter space of stellar population models used in the fitting of the *K*-bright sample, where t_H corresponds to the age of the Universe at a given redshift.

τ-model parameters	
e-folding time	$0.1 < \tau < 10$ Gyr
Age	0.01 Gyr $< t < t_H$
Metallicity	$0.2 < Z < 2.5\,Z_{\odot}$
Reddening	$0.0 < A_V < 3.0$ mag
DB model parameters	
Old comp metallicity	$0.2\,Z_{\odot}, Z_{\odot}$
Old comp age	0.5 Gyr $< t_{\rm oc} < t_H$
Young comp metallicity	$0.2 < Z < 2.5\,Z_{\odot}$
Young comp age	$0.01 < t_{\rm yc} < 0.5$ Gyr
Young comp mass fraction	$0.0 < m_{\rm yc} < 1.0$
Reddening	$0.0 < A_V < 3.0$ mag

dust attenuation law. In addition to providing improved flexibility, the DB models offer the advantage of providing an estimate of the likely maximal stellar mass and age for each member of the *K*-bright sample.

3.1.3 Model fitting procedure

For each member of the *K*-bright sample, the stellar population models were initially shifted to the appropriate redshift and the corresponding FORS2 spectrum was binned up to match the resolution of the stellar population model (typically 10 Å per pixel). The stellar population models were then simultaneously fitted to the spectra and the accompanying *BVYJHK* and IRAC 3.6 and 4.5 μm photometry. During the fitting process, the FORS2 spectral data in the wavelength range 6200–9600 Å were included in the fit, but the wavelength range 9600–10 000 Å was excluded to ensure that bad sky-line residuals did not dominate the fit. The photometric data covering the same wavelength range as the spectra (*Riz*) were not included in the fitting process, simply because those photometric bands had already been used to flux normalize the spectra and photometric data sets.

The photometric broad-band magnitudes were converted to flux densities at the effective wavelength of each filter and the corresponding model predictions were calculated by integrating the models over the appropriate filter profiles. Based on the parameter space outlined in Table 1 , each galaxy was fitted using a grid of up to $\sim 5 \times 10^5$ models from both the BC03 and CB07 libraries. The best-fitting model was determined using χ^2 minimization, with the photometry weighted using the appropriate photometric errors and the spectral data weighted using the FORS2 error spectra.

In order to prevent the fitting procedure from being dominated by the spectral data two key steps were necessary. First, it was necessary to mask areas of the spectra which the spectral synthesis models were not capable of reproducing (principally the [O II] emission line). Secondly, it was necessary to ensure that the FORS2 error spectra actually accounted for all the inherent uncertainties present in the data (both random and systematic). The final reduced FORS2 spectrum for each object typically consists of 5 h of on-source integration time, comprised of a stack of 24 individual exposures, each of 12.5 min integration. Consequently, at each spectral pixel it was possible to use these independent flux measurements to calculate the sigma (σ_f) which fully accounted for the variation in measured flux due to shot noise, varying observing conditions and systematic errors such as imperfect sky-line subtraction. By weighting the final FORS2 spectra by the standard error (i.e. $\sigma_f/\sqrt{24}$), it was possible to perform a combined χ^2 fit to the spectra+photometry without either component dominating the fit.

Four examples of the best-fitting model spectral energy distributions (SEDs) are shown in Fig. 2, where the optical galaxy spectra are plotted in black, the error spectra are plotted in green, the photometric data points are plotted in red and the best-fitting models are plotted in grey. For each object, the left-hand panel of each row shows the full fit and the right-hand panel shows a close-up of the fitting region containing the optical spectra. For presentation purposes the optical spectra have been smoothed using a 5 pixel boxcar.

3.1.4 Adopted stellar masses

In Fig. 3, we show the stellar-mass distributions for the *K*-bright sample, as derived using (left-to-right) τ-models and DB models based on the CB07 template libraries, followed by the corresponding τ-models and DB models based on the BC03 template libraries. Although, as expected, the models based on the CB07 templates produce lower stellar-mass estimates than the models based on the BC03 templates (and the τ-models produce lower stellar-mass estimates than the DB models), perhaps the most striking feature of Fig. 3 is the similarity between the resulting stellar-mass distributions. This is highlighted by the fact that even between the two extremes, the median stellar mass of the *K*-bright sample only changes by 0.17 dex. It is clear from Fig. 3 that the TP-AGB phase is not having a significant impact on the derived stellar masses of the *K*-bright sample. Furthermore, the similarity of the derived stellar-mass distributions implies that the proceeding exploration of the size–mass relation at $z \simeq 1.4$ will not be dominated by systematic stellar-mass uncertainties driven by galaxy SED template choice. Armed with this information, throughout the rest of the paper we simply adopt the stellar-mass and age measurements derived from the BC03 τ-models, in order that they can be directly compared to numerous other studies in the literature (see Section 4.5).

3.2 Galaxy size measurements

Measurements of the galaxy radii were derived using two-dimensional modelling of the latest (DR8) *K*-band imaging of the UDS which has a 5σ detection limit of $K = 24.7$ (2 arcsec diameter apertures) and 0.75 arcsec FWHM image quality. Over the redshift range covered by the *K*-bright sample ($1.3 \leq z \leq 1.5$), the UDS *K*-band imaging is centred on rest-frame wavelengths of $8800 < \lambda < 9600$ Å, which is advantageous for two reasons. First, at these rest-frame wavelengths the *K*-band imaging provides a size measurement significantly long-ward of the 4000 Å break, where the galaxy SED should be relatively unaffected by any recent episodes of star formation. Secondly, at $z \simeq 1.4$ the UDS *K*-band imaging provides size measurements well matched in terms of rest-frame wavelength to the benchmark galaxy size measurements from Shen et al. (2003), which are based on *z*-band SDSS imaging.

The galaxy radii were calculated using a modified version of GALAPAGOS (Barden et al. 2012) and GALFIT (Peng et al. 2002). GALAPAGOS is a wrapper script for GALFIT which fits single Sérsic profiles to each object in the image, taking initial parameters from a catalogue generated by SEXTRACTOR (Bertin & Arnouts 1996). A key advantage of GALAPAGOS compared to GALFIT alone is that it has an algorithm for background estimation and, if necessary, will

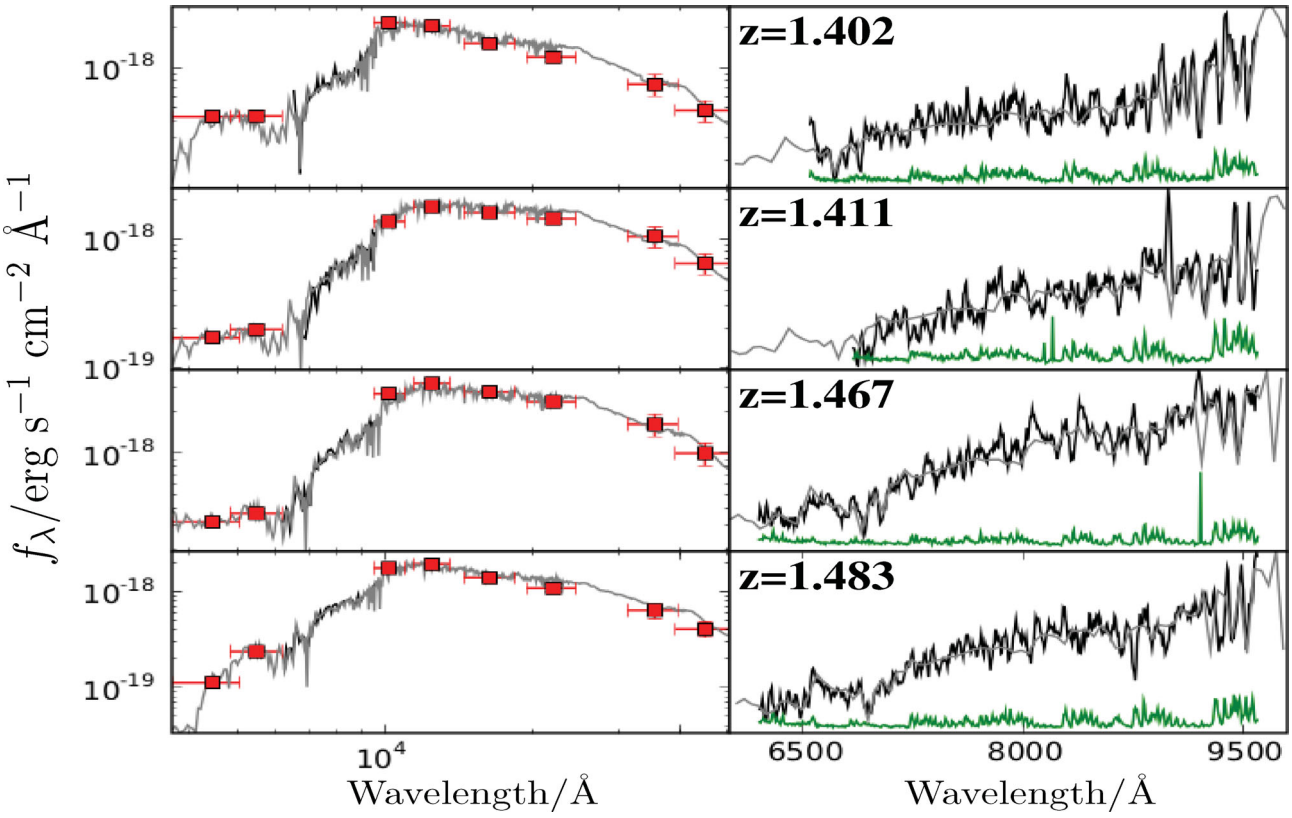

Figure 2. Plots illustrating the spectro-photometric fitting process for four example objects from the *K*-bright sample. The left-hand panels show the combined fits to the spectra and photometry, while the right-hand panels show the model fits through the spectra in detail. In each case, the optical spectrum is shown in black, the error spectrum is shown in green, the photometry is in red and the best-fitting model is in grey. For presentation purposes, the optical spectra have been smoothed using a 5 pixel boxcar.

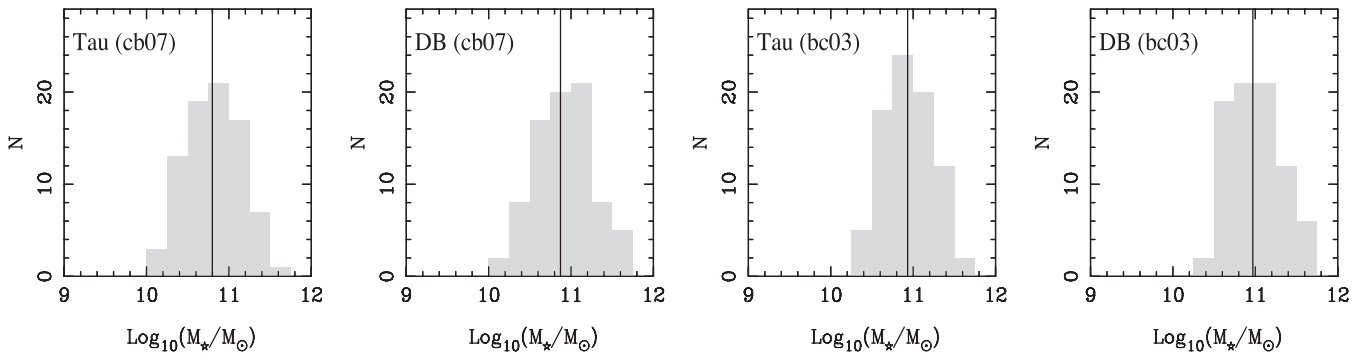

Figure 3. An illustration of the different stellar-mass distributions for the *K*-bright galaxy sample obtained via spectro-photometric fitting based on different stellar population models and SFHs. The stellar-mass distributions are ordered (left-to-right) by increasing median stellar mass (vertical solid lines) and correspond to τ-models and DB models based on the CB07 stellar population models followed by the equivalent models based on the BC03 stellar populations models. From left-to-right the median stellar mass of the sample for each distribution are as follows: 6.3×10^{10}, 7.4×10^{10}, 8.5×10^{10} and 9.3×10^{10} M$_\odot$. For the purposes of the analysis performed in this paper, the stellar-mass measurements derived from the BC03 τ-models have been adopted. However, as illustrated here, the difference in median mass between the extreme combinations of template library/SFH only differ at the 0.17 dex level, insufficient to affect any of the science results derived in the latter sections of the paper.

simultaneously model any nearby companion objects which would otherwise unduly influence the fit.

For this study the code was adapted to produce a densely sampled grid of R_e, Sérsic index and background level in order to estimate accurate errors on the fitted parameters from contours of constant $\Delta\chi^2$. It is worth emphasizing that, because both R_e and Sérsic index correlate with the sky-background level, including a variable background in the parameter estimation grid is essential for obtaining realistic uncertainties on the derived parameters.

3.2.1 Comparison with higher resolution imaging

One approach to testing the accuracy of our galaxy size measurements would be to analyse simulated images containing artificial galaxies spanning a range of half-light radii and Sérsic index. We have not performed such a simulation in this work, simply because building and then reclaiming the properties of artificial galaxies with the same axisymmetric galaxy models is likely to overestimate the accuracy with which the galaxy sizes can be recovered.

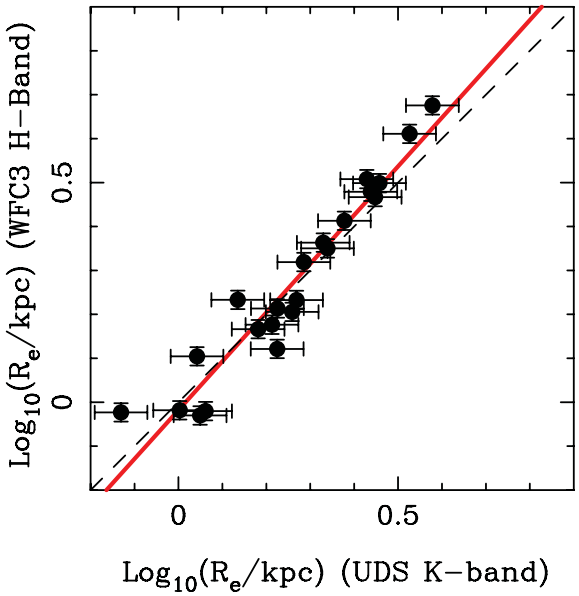

Figure 4. A comparison between the effective half-light radii derived from the ground-based *K*-band imaging and the *HST H*-band imaging for a sample of $N = 22$ objects with $K_{\rm tot} \leq 21.5$ and $1.3 \leq z_{\rm phot} \leq 1.5$ within the CANDELS/UDS field. The thick red line shows the best-fitting relationship (equation 1) and the thin dashed line is a one-to-one relationship (see the text for a full discussion).

However, within the UDS field we are in the fortunate position that it is possible to directly compare galaxy sizes derived from the ground-based and *HST* imaging in the near-IR. Consequently, in order to test whether or not our determinations of the galaxy radii have been affected by the ground-based spatial resolution of the UDS *K*-band imaging, we have made use of the publicly available Cosmic Assembly Near-infrared Deep Extragalactic Legacy Survey (CANDELS; Grogin et al. 2011; Koekemoer et al. 2011) imaging in the UDS. The CANDELS data set in the UDS features *J*- and *H*-band WFC3/IR imaging (FWHM $\simeq$0.2 arcsec) over an area of $\simeq$200 square arcmin to a 5σ depth of 26.8 (0.6 arcsec diameter apertures).

Based on the photometric redshift catalogue of Bruce et al. (2012), there are 22 galaxies within the CANDELS/UDS area with $K_{\rm tot} \leq 21.5$ and photometric redshifts in the range $1.3 \leq z \leq 1.5$. For this sample, the half-light radii and Sérsic index measurements derived by Bruce et al. (2012), based on a GALFIT analysis of the *H*-band *HST* imaging, were compared to those derived using the ground-based *K*-band imaging.

As can been seen from Fig. 4, the results of this comparison demonstrate that the two sets of half-light radii measurements are well correlated ($r_{\rm s} = 0.95$) and follow an essentially one-to-one relation. The best-fitting relation between the two measurements of half-light radius was found to be

$$R_{\rm WFC3} = (0.96 \pm 0.05) R_{\rm UDS}^{1.11 \pm 0.08}, \quad (1)$$

where $R_{\rm WFC3}$ and $R_{\rm UDS}$ are the circularized half-light radii (in kpc) derived from the WFC3/IR and ground-based data, respectively. Moreover, the corresponding Sérsic index measurements were also found to be well correlated ($r_{\rm s} = 0.82$), with only 1/22 objects returning a significantly different best-fitting Sérsic index ($n_{\rm WFC} = 2.0$ versus $n_{\rm UDS} = 3.5$). Consequently, for the purposes of the proceeding analysis, the measurements of half-light radii and Sérsic indices derived from the ground-based *K*-band imaging are adopted without correction.

4 THE STELLAR MASS–SIZE RELATION

In this section, we present the basic results of our study of the galaxy size–mass relation at $z \simeq 1.4$, exploring the location of the *K*-bright sample on the size–mass plane as a function of sSFR, morphology and stellar population age. In what follows, we will consistently compare the results for the *K*-bright sample with the size–mass relations derived by Shen et al. (2003) for early-type ($n \geq 2.5$) and late-type ($n < 2.5$) galaxies in the SDSS. In order to perform this comparison we have converted the semimajor axis half-light radii ($R_{\rm e}$) derived by GALFIT to their equivalent circularized values ($R_{\rm c}$) using the standard conversion: $R_{\rm c} = \sqrt{(b/a)} R_{\rm e}$, where a/b is the best-fitting axial ratio.

In the left-hand panel of Fig. 5, we show the full *K*-bright sample on the size–mass plane. Also shown are the size–mass relations for late-type (thin blue line) and early-type (thick red line) galaxies in the SDSS as derived by Shen et al. (2003), with the dotted lines indicating the 1σ scatter associated with both relations. The shaded region at $M_{\star} \geq 6 \times 10^{10}\,{\rm M}_{\odot}$ highlights the regime where the *K*-bright sample is fully mass-complete. This mass completeness threshold has been calculated in a deliberately conservative manner and is based on a model galaxy at $z = 1.4$ with $K_{\rm tot} = 21.5$, zero current star formation and an age of 4 Gyr. Consequently, at $M_{\star} \geq 6 \times 10^{10}\,{\rm M}_{\odot}$ the *K*-bright sample should be mass-complete, even for entirely passive galaxies. In the stellar-mass interval $3 \times 10^{10} \leq M_{\star} \leq 6 \times 10^{10}\,{\rm M}_{\odot}$, the *K*-bright sample may be partially incomplete for the most passive galaxies, but should still be complete for actively star-forming galaxies, unless they are heavily reddened. The apparent cut-off at stellar masses of $M_{\star} \simeq 3 \times 10^{10}\,{\rm M}_{\odot}$ is thus a function of the adopted $K_{\rm tot} = 21.5$ mag limit and the red colour selection of the FORS2 spectroscopic sample (i.e. $i - K \geq 2$).

4.1 Specific star formation rate

In the right-hand panel of Fig. 5, the *K*-bright sample has been split on the basis of sSFR, where objects with sSFR ≤ 0.1 Gyr^{-1} are plotted as red filled circles and objects with sSFR > 0.1 Gyr^{-1} are plotted as open blue circles. Although it is obviously possible to derive a value of sSFR directly from the best-fitting SED templates, in order to avoid too much coupling between the adopted stellar-mass and SFR measurements, the decision was taken to exploit the different empirical star formation indicators available for the *K*-bright sample.

The first star formation indicator we have employed is the UV luminosity calibration of Madau, Pozzetti & Dickinson (1998) and was based on the observed *B*-band magnitudes, dust corrected using the best-fitting value of $A_{\rm v}$. The second indicator is based on the [O II] emission-line fluxes (or upper limits), and is based on the Kennicutt (1998) calibration assuming that the Hα emission line undergoes an average extinction of 1 mag. The final star formation indicator is based on the observed 24 μm fluxes (or upper limits), which are initially converted into rest-frame 8 μm luminosities using a $10^{11}\,{\rm L}_{\odot}$ starburst template from Lagache, Dole & Puget (2003). Based on the 8 μm luminosity the total IR luminosity is then estimated using the calibration of Bavouzet et al. (2008) and the SFR is estimated using the calibration of Kennicutt (1998).

The adopted SFR estimate for each member of the *K*-bright sample is taken as the *largest* value derived from [O II] emission-line flux, dust-corrected UV luminosity and MIPS 24 μm flux. In this

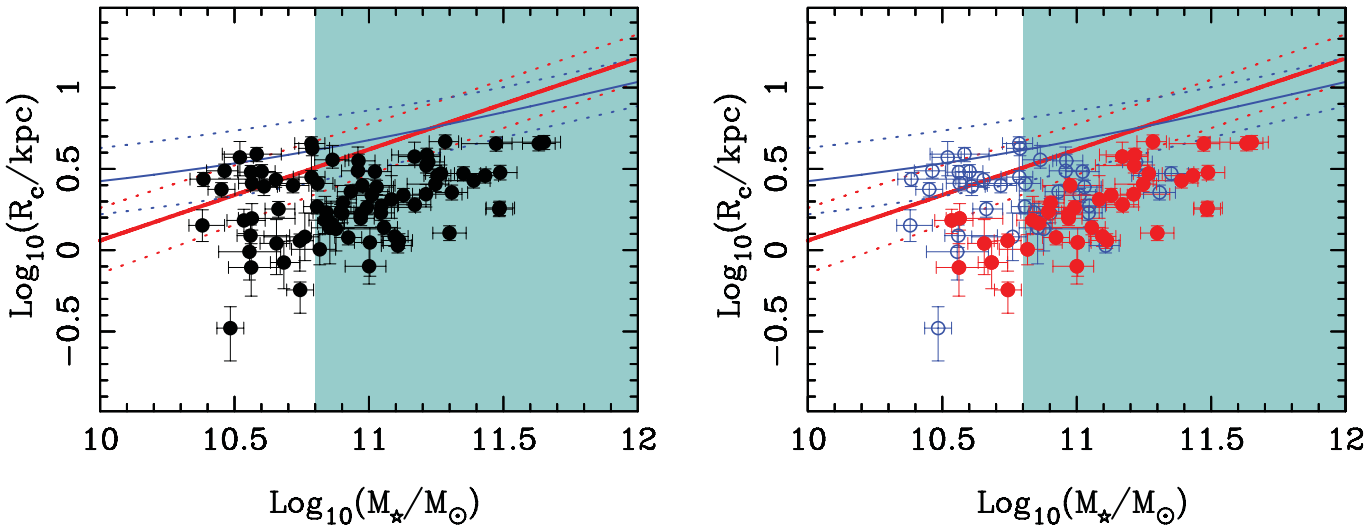

Figure 5. The galaxy size-stellar mass relation for the *K*-bright sample. The left-hand panel shows the location of the *K*-bright sample on the half-light radius and stellar mass plane. The thin (blue) and thick (red) solid lines show the relations derived for $z < 0.1$ SDSS galaxies by Shen et al. (2003) for late-type ($n < 2.5$) and early-type ($n \geq 2.5$) galaxies, respectively (dotted lines indicate the associated 1σ scatter). The shaded region at $\log(M_\star/\mathrm{M}_\odot) \geq 10.8$ highlights where the *K*-bright sample should be 100 per cent mass-complete, even for the most passive galaxies (see the text for discussion). The right-hand panel shows the same information, except that the *K*-bright galaxies have been split into passive (red solid circles) and star-forming (blue open circles) sub-samples depending on whether their sSFR lies above or below 0.1 Gyr^{-1}. In both panels, and all subsequent figures, the plotted half-light radii measurements have been circularized (i.e. $R_\mathrm{c} = \sqrt{(b/a)}R_\mathrm{e}$) in order to facilitate direct comparison with the results of Shen et al. (2003).

fashion, we have deliberately adopted the *maximum* likely value of sSFR for each object, which should ensure that objects with extremely low values of sSFR can be regarded as genuinely passive. The choice of 0.1 Gyr^{-1} as the threshold between actively star-forming and passive objects is motivated by several different factors. Fundamentally, this value is the median sSFR value of the *K*-bright sample and is also a suitable dividing line separating galaxies which are on or off the so-called main sequence of star formation at this epoch (e.g. Elbaz et al. 2011). Moreover, at $z \simeq 1.4$ an sSFR value of 0.1 Gyr^{-1} implies that a galaxy will require a Hubble time in order to double its stellar mass.

4.1.1 *Passive galaxies*

It can clearly be seen from the right-hand panel of Fig. 5 that the passive members of the *K*-bright sample follow a distinct size–mass relation from the actively star-forming members. This point is clarified further in Fig. 6 which shows just the passive members of the *K*-bright sample on the size–mass plane. It is apparent from the left-hand panel of Fig. 6 that the passive members of the *K*-bright sample follow a well-defined size–mass relation, with a slope consistent with the size–mass relation displayed by local ETGs, but with systematically lower half-light radii than their local counterparts.

In this context it is instructive to calculate the size growth factor (f_g), defined here as the increase in half-light radius required to place the *K*-bright galaxies on to the appropriate local galaxy size–mass relation from Shen et al. (2003). To reconcile the passive members of the *K*-bright sample with the local early-type size–mass relation requires a median growth factor of $f_\mathrm{g} = 2.43 \pm 0.20$, even allowing for no increase in stellar mass. This off-set is illustrated by the right-hand panel of Fig. 6, where the local size–mass relation for ETGs derived by Shen et al. (2003) has been lowered in normalization by a factor of $f_\mathrm{g} = 2.43$. Remarkably, it can be seen that this simple re-normalization of the local early-type size–mass relation provides an excellent description of the size–mass relation followed by the passive members of the *K*-bright sample at $z \simeq 1.4$, both in terms of slope and scatter. We will return to this point in Section 5.

4.1.2 *Star-forming galaxies*

In the left-hand panel of Fig. 7, we plot the star-forming (sSFR $>0.1\ \mathrm{Gyr}^{-1}$) half of the *K*-bright sample on the size–mass plane and compare it with the local size–mass relation for late-type galaxies in the SDSS derived by Shen et al. (2003). In contrast to the passive members of the *K*-bright sample, it can immediately be seen that ≃50 per cent of the star-forming galaxies are already consistent with the size–mass relation of local late-type galaxies. As a result, the median value of the growth factor for the star-forming members of the *K*-bright sample is only $f_\mathrm{g} = 1.61 \pm 0.17$,[2] as illustrated in the right-hand panel of Fig. 7.

The results of this sub-section are broadly consistent with many previous studies in the literature (see Section 1) in that, at a given epoch, the off-set from the local size–mass relations is significantly larger for passive galaxies than for their star-forming contemporaries. A detailed comparison with relevant results from the recent literature will be presented in Section 4.5.

4.2 Morphology

When considering the evolution of the galaxy size–mass relation it is conventional to consider the influence of galaxy morphology. Indeed, much of the discussion in the literature has concentrated on the size evolution of morphologically selected ETGs. Consequently, in this section we investigate the size–mass relation for the *K*-bright sample, splitting the sample into late-type and early-type sub-samples using the same Sérsic index threshold of $n = 2.5$ as adopted by Shen et al. (2003).

[2] The outlier at $(\log(M/\mathrm{M}_\odot) = 10.5, \log(R_\mathrm{c}/\mathrm{kpc}) = -0.5)$ has been excluded from this calculation.

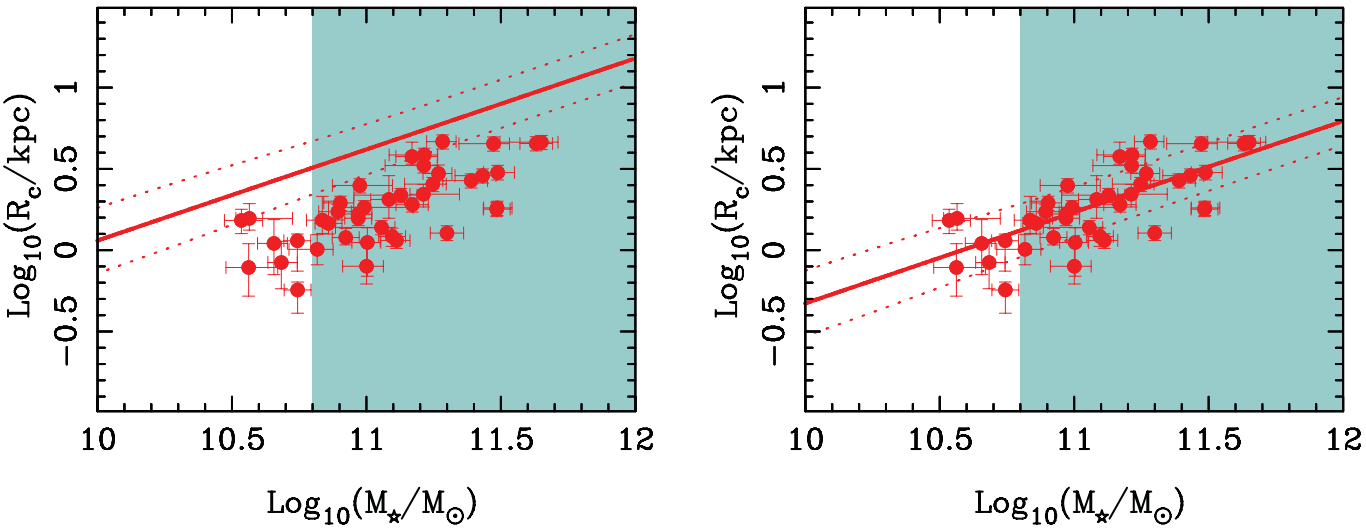

Figure 6. The left-hand panel shows the galaxy size-stellar mass relation for those members of the *K*-bright sample classified as passive according to our adopted sSFR $\leq$0.1 Gyr^{-1} threshold. The solid and dotted lines show the size–mass relation for ETGs in the SDSS derived by Shen et al. (2003) and the corresponding 1σ scatter, respectively. It can be seen that the passive *K*-bright galaxies follow a size–mass relation which has an identical slope (and scatter) to that of local ETGs, but is simply shifted in normalization. This is illustrated by the right-hand panel which shows the effect of reducing the vertical normalization of the Shen et al. early-type relation by a growth factor of $f_{\rm g} = 2.43 \pm 0.20$ (see the text for discussion).

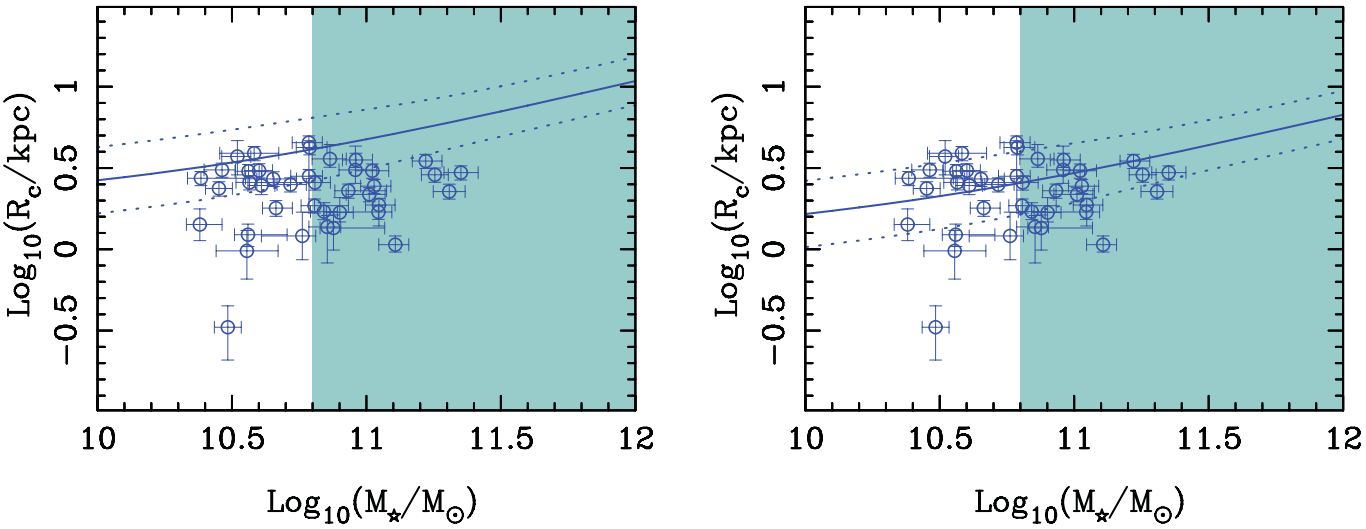

Figure 7. The left-hand panel shows the galaxy size-stellar mass relation for the those members of the *K*-bright sample classified as star forming according to our adopted sSFR $>$ 0.1 Gyr^{-1} threshold. The solid and dotted lines show the size–mass relation for late-type galaxies in the SDSS derived by Shen et al. (2003) and the corresponding 1σ scatter, respectively. It can be seen that the star-forming *K*-bright galaxies are consistent with following a size–mass relation similar to that of local late types, but shifted in normalization. This is illustrated by the right-hand panel which shows the effect of reducing the vertical normalization of the Shen et al. late-type relation by a growth factor of $f_{\rm g} = 1.61 \pm 0.17$ (see the text for discussion).

4.2.1 Early-type galaxies

The middle panel of Fig. 8 shows the size–mass relation for the early-type ($n \geq 2.5$) members of the *K*-bright sample compared to the size–mass relation for local ETGs from Shen et al. (2003). It can be seen that the ETGs follow a size–mass relation which has a slope which is consistent with the local size–mass relation for early types, but is off-set to smaller radii at a given stellar mass. In terms of the growth factor ($f_{\rm g}$), the ETGs are off-set from the local size–mass relation by a factor of $f_{\rm g} = 2.37 \pm 0.29$.

If we confine our attention to the growth factor required to reconcile them with the local size–mass relation for ETGs, it is clear that the passive and early-type sub-samples of the *K*-bright galaxies are very similar, with $f_{\rm g} = 2.43 \pm 0.20$ and 2.37 ± 0.29, respectively. However, it is noticeable that the scatter associated with the size–mass relation displayed by the early-type sub-sample is somewhat larger than that associated with the size–mass relation of the passive galaxy sub-sample. Comparing Fig. 6 with Fig. 8, it is clear that the reason for the increased scatter is that unlike the passive galaxy sub-sample, $\simeq$30 per cent of the early-type sub-sample have half-light radii which are consistent with the local early-type size–mass relation.

Interestingly, although splitting the full *K*-bright sample at $n \geq 2.5$ or sSFR $\leq$0.1 Gyr^{-1} delivers similar sized sub-samples ($N = 37$ and 41 galaxies, respectively), the correspondence

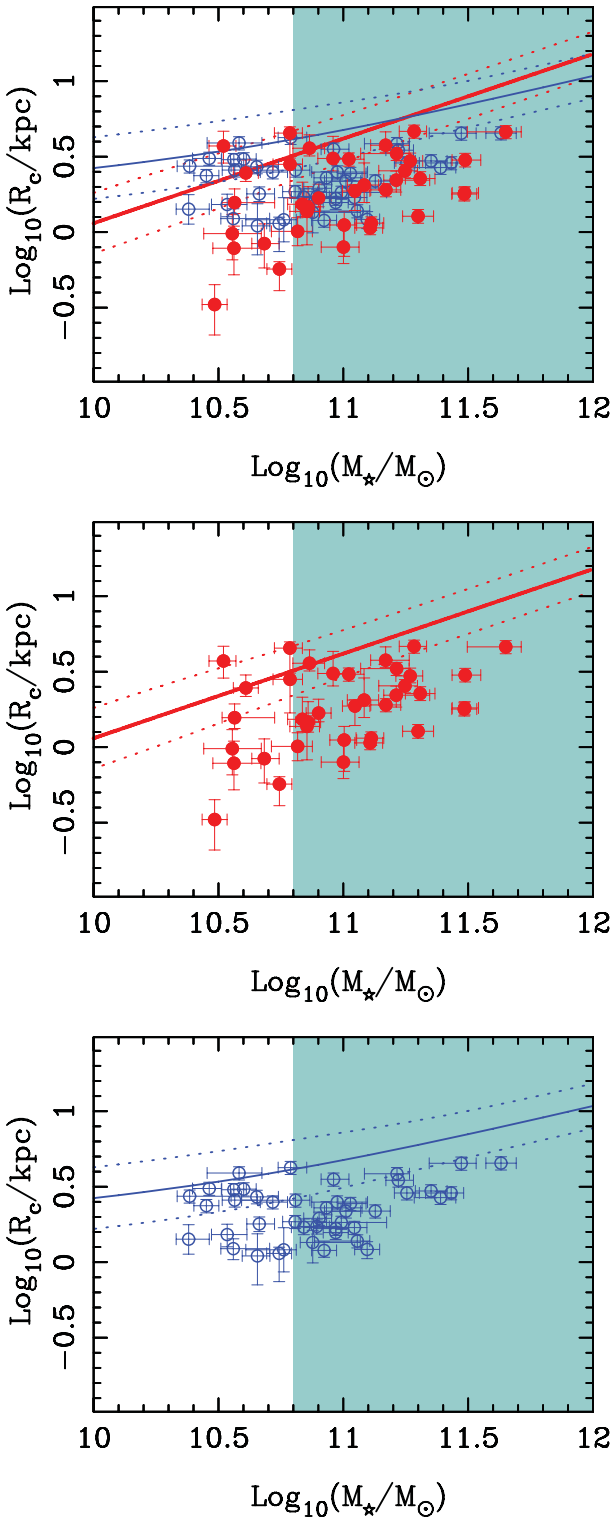

Figure 8. The top panel shows the size–mass relation for the *K*-bright sample with ETGs ($n \geq 2.5$) plotted as solid red circles and late-type galaxies ($n < 2.5$) plotted as open blue circles. The middle panel shows the early-type *K*-bright galaxies compared to the local early-type size–mass relation from Shen et al. (2003). The bottom panel shows the equivalent comparison for the late-type *K*-bright galaxies.

between an early-type morphology and passivity is not one-to-one. Indeed, the 41 galaxies in the *K*-bright sample classified as passive are split relatively evenly between early-type ($N = 23$) and late-type morphologies ($N = 18$). Similarly, of the 37 objects in the early-type sub-sample, only 23 are also classified as passive. Consequently, it is clear that a relatively large fraction (≃20 per cent) of the *K*-bright galaxies are classified as star-forming early-types according to our adopted sSFR and Sérsic index criteria.

4.2.2 *Late-type galaxies*

In the bottom panel of Fig. 8, we plot the size–mass relation for the late-type ($n < 2.5$) members of the *K*-bright sample. As with the early-type sub-sample, the late-type members of the *K*-bright sample appear to follow a size–mass relation which has a slope which is consistent with the equivalent local size–mass relation, but off-set to smaller half-light radii at a given stellar mass. If we calculate the off-set from the local size–mass relation in terms of the growth factor, we derive a median value of $f_g = 2.15 \pm 0.15$.

It is noteworthy that this growth factor is larger than the growth factor previously calculated for the star-forming members of the *K*-bright sample ($f_g = 1.61 \pm 0.17$). Again, the reason for this apparent discrepancy is that the correspondence between late-type morphology and active star formation is not one-to-one. In fact, of the 44 members of the late-type sub-sample, 26 are actively star-forming galaxies and 18 are galaxies which are classified as passive according to our adopted sSFR threshold. The overall growth factor of $f_g = 2.15 \pm 0.15$ is therefore effectively an average of the $f_g = 1.79 \pm 0.17$ displayed by the star-forming late-type galaxies and the significantly larger growth factor of $f_g = 2.48 \pm 0.23$ displayed by the *passive* late-type galaxies.

Therefore, not only is ≃20 per cent of the *K*-bright sample comprised of star-forming bulges which are *larger* than their passive counterparts, a further ≃20 per cent is comprised of passive disc-like galaxies which are *smaller* than their actively star-forming counterparts. In combination with the tight size–mass correlation displayed by the passive sub-sample in Fig. 5, this information leads naturally to the conclusion that the location of massive $z \simeq 1.4$ galaxies on the size–mass plane is a stronger function of sSFR than galaxy morphology.

Finally, it is interesting to note that ≥40 per cent of the passive members of the *K*-bright sample are classified as having a disc-like morphology (i.e. $n < 2.5$). This result provides potentially important information about the quenching of star formation in massive galaxies and will be discussed in more detail in Section 5.

4.3 Stellar population age

In this section, we examine the evidence for a relationship between galaxy size and stellar population age within the early-type/passive members of the *K*-bright sample, given that the confirmation of any such relationship would offer important constraints on competing evolutionary scenarios. Recent results on this issue in the literature have been controversial, with different studies finding apparently contradictory claims (e.g. Saracco et al. 2009; Trujillo et al. 2011). In the following discussion, we have adopted the best-fitting age since formation (t_{for}) as our age indicator, although quantitatively similar results are derived if the alternative age indicator t_{for}/τ is employed.

4.3.1 Passive galaxies

The median age of the passive galaxy sub-sample is 3.3 ± 0.2 Gyr, which is consistent with a formation redshift of $z_{\rm for} \simeq 4.5$. If we divide the sample into 'old' and 'young' based on this median age, then the passive sub-sample also cleanly separates in terms of half-light radius and stellar mass. For example, the median stellar mass of the 'old' passive galaxies is $M_\star = (1.64 \pm 0.29) \times 10^{11}\,{\rm M}_\odot$, whereas the median stellar mass of the 'young' passive galaxies is $M_\star = (0.79 \pm 0.21) \times 10^{11}\,{\rm M}_\odot$. The corresponding median values for the half-light radii are 2.52 ± 0.35 kpc for the 'old' passive sub-sample and 1.55 ± 0.22 kpc for the 'young' passive sub-sample.

Several aspects of these results are noteworthy. First, the fact that the oldest passive members of the *K*-bright sample are systematically more massive than the youngest passive members indicates that the process of 'downsizing' is already in place for massive galaxies at $z \simeq 1.4$. Moreover, the difference in median half-light radius for the 'old' and 'young' passive galaxies is entirely consistent with the correlation between half-light radius and stellar mass seen for ETGs in the SDSS by Shen et al. (2003), i.e. $r_{\rm hl} \propto M^{0.56}$ (as expected given the relation shown in Fig. 6).

Therefore, although we do find a factor of $\simeq$1.6 difference in the median half-light radii of the 'old' and 'young' passive galaxy sub-samples, this is simply a consequence of the correlations between size–mass and mass–age. Indeed, because the passive galaxy sample follows a size–mass relation with an identical slope to that seen at low redshift (see Fig. 6), the median growth factors of the 'old' and 'young' members of the passive galaxy sub-sample are perfectly consistent ($f_{\rm g} = 2.39 \pm 0.32$ and 2.41 ± 0.26, respectively). Based on this evidence, we conclude that there is no correlation between stellar population age and off-set from the local size–mass relation for passive galaxies within the *K*-bright sample (see Section 5 for further discussion).

4.3.2 Early-type galaxies

A more direct comparison with existing studies in the literature is to examine if there are any correlations with stellar population age within the early-type ($n \geq 2.5$) members of the *K*-bright sample.

To explore this issue, we adopt the same simple strategy and split the early types into 'young' and 'old' sub-samples using the median age since formation (which is again 3.3 Gyr). If we then calculate the median growth factor needed to reconcile the *K*-bright early types with the local early-type size–mass relation we derive values of $f_{\rm g} = 2.50 \pm 0.32$ for the 'old' sub-sample and $f_{\rm g} = 2.28 \pm 0.46$ for the 'young' sub-sample. As for the passive members of the *K*-bright sample, based on these results we conclude that there is no indication that the off-set from the local early-type size–mass relation is related to stellar population age at $z \simeq 1.4$ (consistent with the conclusions of Cimatti et al. 2012). In fact, as with the passive sub-sample, the median half-light radius of the 'old' ETGs is actually larger than that of the 'young' early types (2.2 ± 0.3 versus 1.6 ± 0.3 kpc), as a result of the correlation between stellar population age and stellar mass.

4.4 Dynamical-mass measurements

For a 13-object sub-sample of the *K*-bright galaxies, it was possible to extract a reliable measurement of their stellar-velocity dispersion. Consequently, for this small sub-sample it is possible to derive dynamical-mass estimates and thereby provide an independent measurement of the typical size evolution, free from the systematic uncertainties associated with stellar-mass measurements based on SED fitting. The sub-sample of galaxies with stellar-velocity-dispersion measurements is confined to those objects which were bright enough to provide the necessary signal-to-noise ratio (i.e. SNR $\simeq$8 per pixel) and to the redshift interval $1.30 \leq z \leq 1.41$, such that the strong Ca H&K absorption features lie within a clean region of spectrum, clear of strong sky-line residuals.

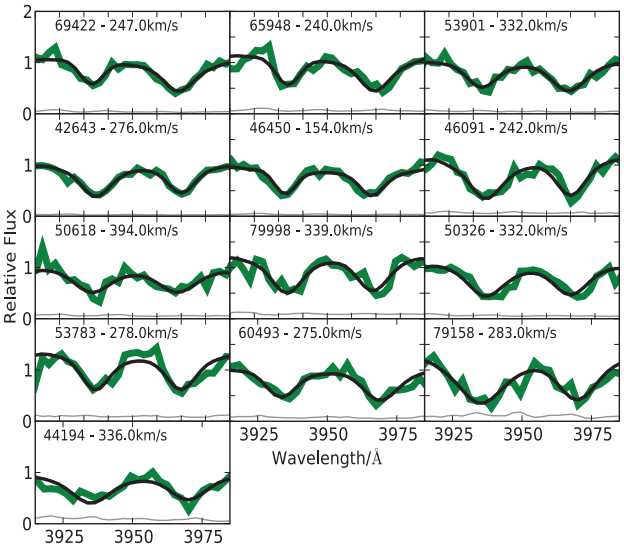

Figure 9. Illustration of the model fitting employed to derive stellar-velocity dispersions for 13 galaxies with sufficiently high signal-to-noise ratio (SNR $\simeq$8 per pixel) in the Ca H&K spectral region. In each panel the thick green line is the galaxy spectrum, the black line is the best-fitting convolved stellar spectrum and the thin grey line is the error spectrum. The catalogue ID number and best-fitting stellar-velocity dispersion are shown at the top of each panel.

The velocity dispersions were measured via χ^2 minimization in pixel space, using a template library of 215 high SNR stellar spectra taken from STELIB stellar library (Le Borgne et al. 2003), as illustrated in Fig. 9. The corresponding dynamical mass estimates were derived using the following expression:

$$M_{\rm dyn} = \frac{5\sigma^2 R_{\rm c}}{G}, \qquad (2)$$

where $R_{\rm c}$ is the circularized half-light radius and σ is the line-of-sight velocity dispersion within the half-light radius (aperture corrected according to Jorgensen et al. 1996).

4.4.1 Size evolution

Based on the relationship between half-light radius and dynamical mass derived for early-type SDSS galaxies by van der Wel et al. (2008), it is possible to predict the $z = 0$ half-light radius of a galaxy with a given dynamical mass. Therefore, for each *K*-bright galaxy with a measured velocity dispersion it is possible to calculate the ratio of the observed half-light radius at $z \simeq 1.4$ to the expected half-light radius at $z = 0$ for a galaxy of the same dynamical mass.

In Fig. 10, we show the results of this calculation for the 13 *K*-bright galaxies with velocity-dispersion measurements. In Fig. 10, we also show the van der Wel et al. (2008) sample of 50 ETGs, consisting of both $z \simeq 1$ field galaxies and cluster galaxies at $z = 0.831$, and the results from Newman et al. (2010) for 17 ETGs in

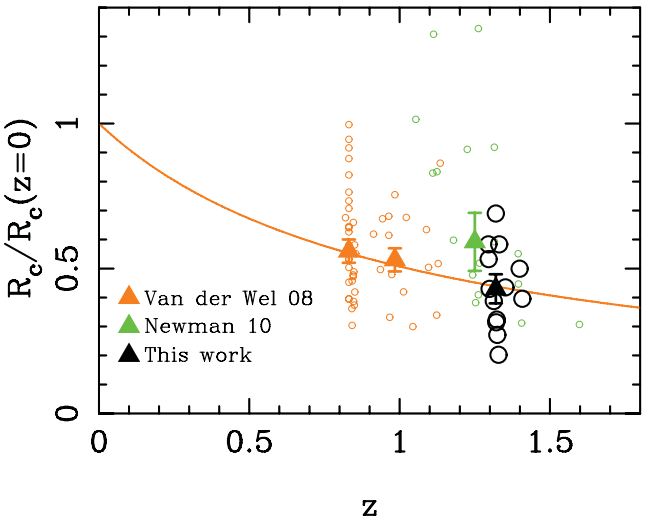

Figure 10. The evolution of circularized effective radius as a function of redshift for ETGs with dynamical-mass estimates of $M_{\rm dyn} \simeq 10^{11}$ M$_\odot$, normalized to the dynamical-mass–size relation determined from the SDSS by van der Wel et al. (2008); see the text for details. The orange data points are taken from the sample of 50 ETGs published by van der Wel et al. (2008), which contains both field galaxies at $z \simeq 1$ and cluster galaxies at $z = 0.831$. The green data points are a sample of 17 early-type field galaxies in the redshift interval $1.054 \leq z \leq 1.598$ with velocity-dispersion measurements derived from Keck spectroscopy published by Newman et al. (2010). The black data points are the 13 galaxies from the *K*-bright sample for which it was possible to obtain velocity-dispersion measurements and therefore dynamical-mass estimates. In each case the filled triangles with error bars indicate the sample medians. The solid curve shows the evolutionary trend derived by van der Wel et al. (2008) which has the functional form $R_{\rm c}(z) \propto (1+z)^{-0.98 \pm 0.11}$. In order to agree with the velocity-dispersion normalization adopted both here and in van der Wel et al. (2008), the velocity-dispersion measurements of Newman et al. (2010) have been corrected to match the velocity dispersion within the half-light radius according to the prescription outlined in Jorgensen, Franx & Kjaergaard (1996).

the redshift interval $1.054 \leq z \leq 1.598$. The solid curve shown in Fig. 10 is the best-fitting relation for the observed half-light radius evolution from van der Wel et al. (2008) which has the form $R_{\rm c}(z) \propto (1+z)^{-0.98 \pm 0.11}$.

It can be seen from Fig. 10 that the results derived here are in good agreement with those derived by van der Wel et al. (2008) and Newman et al. (2010). Moreover, using the median value of $R_{\rm c}/R_{\rm c(z=0)}$ for the *K*-bright sub-sample with dynamical-mass measurements we can derive an independent estimate of the growth factor needed to reconcile the sizes of the *K*-bright galaxies with their local counterparts. It is encouraging that the resulting value of $f_{\rm g} = 2.33 \pm 0.32$ is fully consistent with our measurements derived on the basis of the stellar-mass–size relation.

4.5 Comparison with the literature

Given the extensive body of work dealing with the size evolution of massive galaxies already in the literature, it is clearly impossible to comprehensively compare our results with every relevant paper on the subject. Consequently, in this sub-section we have chosen to compare our results with four representative papers which cover the same redshift and stellar-mass range as the *K*-bright sample.

4.5.1 Trujillo et al. (2007)

Trujillo et al. (2007) analysed the sizes of massive ($M_\star \geq 10^{11}$ M$_\odot$) galaxies in the redshift interval $0.2 < z < 2.0$, based on a sample of 810 *K*-band-selected galaxies in the Palomar/DEEP-2 survey. Using stellar-mass estimates based on the BC03 stellar population models (Chabrier IMF) and circularized half-light radii derived from the available F814W ACS imaging, Trujillo et al. observed rapid size evolution in both the massive late-type ($n < 2.5$) and early-type ($n \geq 2.5$) galaxy populations. Given that the Trujillo et al. sample is *K*-band selected, adopts the same SED fitting models and covers the same stellar-mass range as the *K*-bright sample, it is clearly of interest to compare their size evolution results with those derived here.

A precise comparison is slightly problematic because the redshift range spanned by the *K*-bright sample ($1.3 \leq z \leq 1.5$) straddles two of the redshift bins adopted by Trujillo et al. ($1.1 < z < 1.4$ and $1.4 < z < 1.7$). However, if we simply adopt the average of the results for the two Trujillo et al. redshift bins, their results suggest that at $z \simeq 1.4$ the growth factor for late-type galaxies is $f_{\rm g} \simeq 1.8$ and the growth factor for ETGs is $f_{\rm g} \simeq 3.3$. Exactly the same growth factors are obtained if we instead adopt the fitting formulas derived by Buitrago et al. (2008), who incorporated the Trujillo et al. (2007) results in their study of the size evolution of massive galaxies over the redshift interval $0.0 < z < 3.0$. These figures are to be compared with the results presented in Section 4.2, which were $f_{\rm g} = 2.15 \pm 0.15$ for late types and $f_{\rm g} = 2.37 \pm 0.29$ for early types.

It is clear from this comparison that while our results for massive late-type galaxies are in reasonable agreement, our determination of the size evolution for massive ETGs at $z \simeq 1.4$ is significantly smaller than derived by Trujillo et al. (2007). However, in reality, the locus of the *K*-bright ETGs on the size–mass plane is entirely consistent with the Trujillo et al. sample (e.g. their fig. 7). The fundamental reason for the difference in derived growth factors is simply that the *K*-bright sample does not display the significant ($\simeq 20$ per cent) tail of objects with $R_{\rm c} \leq 1$ kpc which is present in the Trujillo et al. (2007) sample. It is possible that the lack of $R_{\rm c} \leq 1$ kpc objects in the *K*-bright sample is associated with the limitations of ground-based imaging, although our comparison to the available WFC3/IR imaging (see Section 3.2.1) suggests that the *K*-band $R_{\rm c}$ determinations are reliable down to $\simeq$1 kpc and there is no indication of a 'plateau' in the $R_{\rm c}$ values shown in Fig. 6.

4.5.2 Saracco et al. (2009)

Saracco et al. (2009) investigated the massive galaxy size–mass relation using *H*-band *HST* NICMOS imaging of a heterogeneous sample of 32, morphologically classified, ETGs in the redshift interval $1 < z < 2$. Based on the available 0.4–2.2 μm photometry, Saracco et al. (2009) performed SED fitting using the BC03 template library (Chabrier IMF) and exponentially decaying SFHs. Consequently, it is straightforward to directly compare the results of Saracco et al. (2009) with those derived here.

Based on their SED fitting, Saracco et al. found that their sample of ETGs displayed a bi-model distribution of ages, with peaks at $\simeq$1 and $\simeq$3.5 Gyr, respectively. Splitting their sample into old ETGs (oETGs) and young ETGs (yETGs) using an age threshold of 2 Gyr, Saracco et al. found that while $z \simeq 1.5$ oETGs have half-light radii which are a factor of $\simeq$2.5 smaller than their local counterparts, yETGs at $z \simeq 1.5$ are fully consistent with the local size–mass relation. As already discussed in Section 4.3, amongst the

early-type ($n \geq 2.5$) members of the *K*-bright sample we find no evidence that the off-set from the local size–mass relation is a function of stellar population age, instead finding that sSFR is the fundamental physical parameter which determines the location of massive $z \simeq 1.4$ galaxies on the size–mass plane.

In light of this apparent contradiction, it is clearly of interest to ask whether we can reproduce the results of Saracco et al. if we employ the same criteria to separate the *K*-bright sample. Specifically, if we identify old early types on the basis of $n \geq 2.5$ and a best-fitting stellar population age $\geq$2 Gyr, we find that the *K*-bright sample contains 29 such galaxies. Notably, within this sub-sample of oETGs 22/29 (76 per cent) would also be classified as passive according to our adopted sSFR threshold of $\leq$0.1 Gyr^{-1}. Moreover, if we identify yETGs in the *K*-bright sample as having $n < 2.5$ and age <2 Gyr, we find that 7/8 (88 per cent) of the galaxies satisfying these criteria would also be classified as actively star forming according to our sSFR > 0.1 Gyr^{-1} criterion.

Based on the results derived here, we would therefore expect that separating the Saracco et al. (2009) sample into oETGs and yETGs should produce a size–mass plot which looks similar to the right-hand panel of Fig. 5. Specifically, we would expect that the oETGs should closely mimic our passive galaxy sub-sample, following a size–mass relation with a normalization factor of $\simeq$2.5 lower than the local early-type size–mass relation. Furthermore, we would expect the yETGs to mimic our star-forming sub-sample, lying on the local early-type size–mass relation at $\log(M/\mathrm{M}_{\odot}) < 10.8$, but lying a factor of $\simeq$2 below it at $\log(M/\mathrm{M}_{\odot}) \geq 10.8$. If we examine the results derived by Saracco et al. (e.g. their fig. 9) it can be seen that their sub-samples of yETGs and oETGs display exactly the expected behaviour.

Consequently, we conclude that the Saracco et al. (2009) results are entirely consistent with sSFR being the fundamental physical parameter governing the location of massive galaxies on the size–mass plane and that, amongst morphologically selected ETGs at $1 < z < 2$, a stellar population age $\geq$2 Gyr is a reasonable, but not one-to-one, proxy for passivity.

4.5.3 *Williams et al. (2010)*

Williams et al. (2010) studied the size evolution of massive galaxies at $z_{\mathrm{phot}} \leq 2$, using a sample of $\simeq$30 000 ($K < 22.4$) galaxies selected from the first data release of the UDS. The stellar-mass estimates derived by Williams et al. were based on the BC03 template library and assume a Chabrier IMF, again making the comparison of their results with those derived here straightforward.

In comparison to the Williams et al. sample, the *K*-bright sample has the advantage of spectroscopic redshifts, significantly deeper photometry in the range 1.0–4.5 μm and full spectro-photometric fitting of the combined photometry and FORS2 spectra. However, in contrast, the Williams et al. sample is $\simeq$350 times larger than the *K*-bright sample and covers a wider redshift range.

As part of their investigation, Williams et al. split their sample into passive and star-forming galaxies using an sSFR threshold of sSFR $= 0.3/t_H$, where t_H is the age of the Universe at a given redshift. Notably, over the redshift range spanned by the *K*-bright sample ($1.3 \leq z \leq 1.5$) this threshold in sSFR is virtually identical to the alternative threshold of sSFR $= 0.1$ Gyr^{-1} adopted here. Over the redshift interval $0.5 < z_{\mathrm{phot}} < 2.0$, Williams et al. find that the evolution of the median half-light radii of massive ($\log(M/\mathrm{M}_{\odot}) \geq 10.8$) passive galaxies evolves as $\log(R_{\mathrm{c}}) = 0.78(1+z)^{-1.17}$.

Consequently, at the median redshift of the *K*-bright sample, the results of Williams et al. would predict that the median circularized half-light radius of passive *K*-bright galaxies with $\log(M/\mathrm{M}_{\odot}) \geq 10.8$ should be 1.9 ± 0.1 kpc. This is in excellent agreement with the equivalent value of $R_{\mathrm{c}} = 1.93 \pm 0.24$ kpc we derive for the passive members of the *K*-bright sample.

4.5.4 *van Dokkum et al. (2010)*

In an effort to avoid the effects of progenitor bias, van Dokkum et al. (2010) used the NEWFIRM medium-band survey to select galaxies with a constant number density of $n = 2 \times 10^{-4}$ Mpc^{-3} over the photometric redshift interval $0.2 < z < 2.2$. In each of four redshift bins, stacked images of the selected galaxies were used to increase the SNR and allow the evolution of the typical galaxy structural parameters to be measured. Over the redshift interval $0 < z < 2.2$, van Dokkum et al. (hereafter vD10) found that massive galaxies selected to have a constant number density of $n = 2 \times 10^{-4}$ Mpc^{-3} display a factor of $\simeq$4 growth in their effective radius, but that the corresponding growth in their stellar mass is only a factor of $\simeq$2. As noted by vD10, these results are in agreement with a galaxy growth model based on minor mergers (see Section 5), a conclusion further supported by their finding that the additional stellar-mass growth occurs predominantly at large galactic radii (i.e. $r > 5$ kpc).

Given that vD10 do not split their sample into early and late-type morphologies, it is interesting to compare their results with our results for the full *K*-bright sample, independent of morphological or sSFR thresholds. Based on their fitting functions for the evolution of stellar mass, vD10 would predict that galaxies with a constant number density of $n = 2 \times 10^{-4}$ Mpc^{-3} at $z \simeq 1.4$ should have a median stellar mass of $\log(M/\mathrm{M}_{\odot}) = 11.24$. The stellar masses for the vD10 sample were calculated assuming a Kroupa IMF and the Maraston et al. (2005) stellar population models. If we adopt the conversions calculated by Cimatti et al. (2008), we see that a stellar mass of $\log(M/\mathrm{M}_{\odot}) = 11.24$ is equivalent to $\log(M/\mathrm{M}_{\odot}) = 11.35$ assuming a Chabrier IMF and the BC03 stellar population models. If we then adopt the vD10 policy and define our mass bin as 11.35 ± 0.15, we identify a sample of 17 galaxies within the *K*-bright sample. The corresponding number density of this sub-sample is $n = (1.5 \pm 0.4) \times 10^{-4}$ Mpc^{-3}, in good agreement with the vD10 expectation. However, our results indicate that the median effective half-light radius (semimajor axis) of this sub-sample is 3.3 ± 0.3 kpc, approximately 25 per cent smaller than the vD10 result of 4.3 ± 0.3 kpc.

5 DISCUSSION

In this final section, we provide an extended discussion of the two most important results of this study. First, we explore whether any of the commonly proposed evolutionary mechanisms can plausibly explain the observed size–mass evolution of the passive members of the *K*-bright sample, given the available observational and theoretical constraints. Secondly, we discuss the implications for the quenching of star formation in massive galaxies at high redshift given our result that a substantial fraction of the passive members of the *K*-bright sample at $z \simeq 1.4$ have disc-like morphologies.

5.1 Mechanisms for galaxy size evolution

Perhaps the cleanest result to emerge from this study is that the passive (sSFR $\leq$0.1Gyr^{-1}) members of the *K*-bright sample follow a size–mass relation which is identical in slope (and scatter) to that followed by ETGs in the SDSS, but off-set to smaller half-light

radii by a factor of ≃2.4. As a consequence, in this sub-section we investigate whether any of the commonly discussed evolutionary mechanisms are capable of reconciling the size–mass relations for passive galaxies at $z \simeq 1.4$ and $z \simeq 0$, without violating other observational constraints at low redshift.

In the following discussion, we assume that the additional stellar mass added by on-going star formation amongst the passive galaxy sub-sample is negligible. Making the conservative assumption that the typical SFR remains constant between the observed epoch and the present day, the fractional increase in stellar mass from on-going star formation is $\simeq t_{LB} \times \langle \mathrm{sSFR} \rangle$. Taking the median values for the passive galaxy sub-sample implies that the fractional increase in stellar mass is only ≃18 per cent (0.07 dex).

5.1.1 AGN feedback

It has been proposed in the literature that mechanical feedback from AGN could be responsible for increasing the size of massive, compact galaxies at high redshift (e.g. Fan et al. 2008). In this scenario, AGN-driven outflows are responsible for evacuating material from the central regions of compact galaxies, resulting in an increase in half-light radius and a decrease in the central stellar-velocity dispersion. In fact, because the total mass is conserved, the initial and final values of the half-light radius and stellar-velocity dispersion are related as follows: $\sigma_\mathrm{f}/\sigma_\mathrm{i} = (R_\mathrm{f}/R_\mathrm{i})^{-1/2}$.

Using the dynamical-mass measurements for the *K*-bright galaxies derived here, it is not possible to rule out the AGN feedback mechanism as a viable explanation of the observed size evolution. For example, the median stellar mass of the *K*-bright sub-sample with dynamical-mass measurements is $M_\star \simeq 10^{11}\,\mathrm{M}_\odot$ and the median stellar-velocity dispersion is $\sigma_\mathrm{med} = 275$ km s^{-1}. Consequently, if their size growth is assumed to be due to AGN feedback, the prediction would be that SDSS galaxies with stellar masses of $M_\star \simeq 10^{11}\,\mathrm{M}_\odot$ should have stellar-velocity dispersions of $\sigma \simeq 180$ km s^{-1}. This is consistent with what is actually observed for ETGs in the SDSS (e.g. van Dokkum, Kriek & Franx 2009).

However, there are several features of the results derived here which suggest that AGN feedback is not the dominant mechanism responsible for the size evolution of compact high-redshift galaxies. The first is our finding that at $z \simeq 1.4$ the off-set from the local size–mass relation is not a function of stellar population age. The second is that we find no indication that the scatter in the galaxy size–mass relation is significantly greater at $z \simeq 1.4$ than it is locally. Both of these results run counter to the expectations of the AGN feedback model as already highlighted by Trujillo et al. (2011), based on their study of the size–mass relation of massive ETGs at $z \simeq 1$. Moreover, recent numerical simulations suggest that the greatest impact of AGN feedback is likely to occur in much younger stellar populations than the ≥1 Gyr old populations seen in massive galaxies at $z \simeq 1.5$ (Ragone-Figueroa & Granato 2011). Finally, it would also appear unlikely that AGN feedback activity can play an important role in compact galaxies with low sSFR, given that these galaxies presumably no longer contain a large reservoir of gas.

5.1.2 Major mergers

Ever since the initial evidence began to emerge that a population of seemingly old, highly compact, ETGs existed at $z \geq 1$, the prospect of explaining their subsequent evolution via a sequence of major dry (i.e. dissipationless) mergers has been widely discussed in the literature. This scenario is immediately appealing because the product

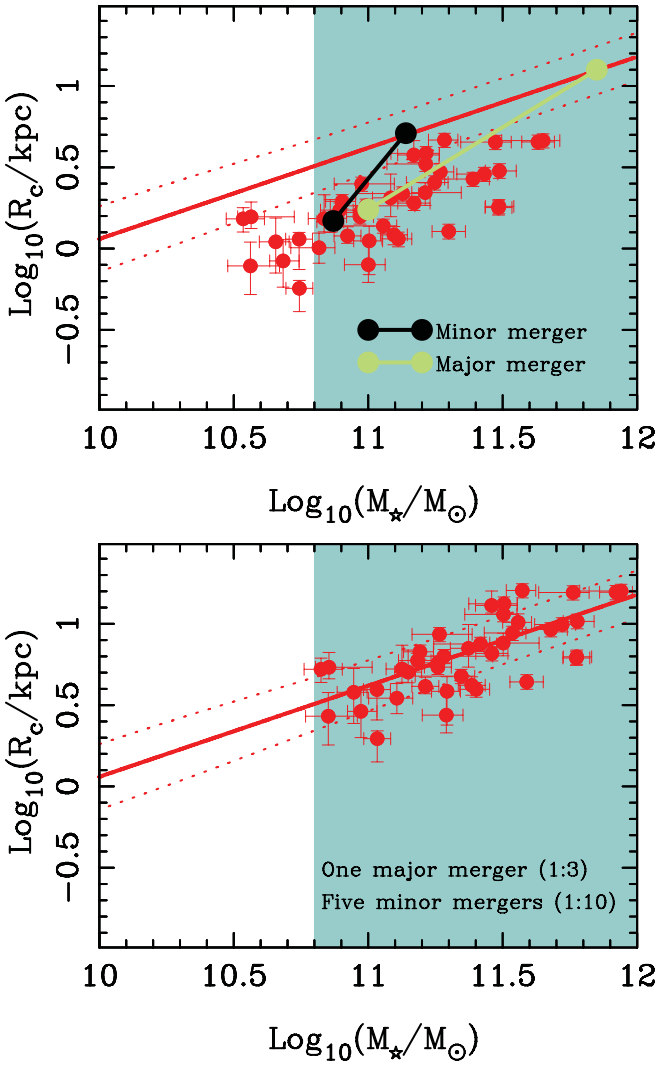

Figure 11. The top panel shows the size–mass relation for the passive members of the *K*-bright sample, together with the local early-type size–mass relation from Shen et al. (2003). The connected black and green points illustrate the evolutionary path followed by galaxies if they undergo minor and major mergers, respectively. The bottom panel shows the final location of the passive *K*-bright galaxies if they evolve according to our chosen toy model, which consists of a single major merger (mass ratio 1:3) and five minor (mass ratio 1:10) mergers (see the text for a full discussion).

of a major (i.e. mass ratio ≥1:3) dry merger is expected to have an early-type morphology with a half-light radius which has increased proportionally to the increase in stellar mass (e.g. Naab et al. 2009). In Fig. 11, the green line illustrates the evolutionary path which would be followed by a member of the *K*-bright sample if its size evolution is driven by major mergers.

Although appealing, there are two obvious problems with the major-merger scenario which would appear to exclude it as the dominant mechanism responsible for the size evolution of compact high-redshift galaxies. First, there is the problem of the number of major mergers that are actually required to reconcile the observed size–mass relations at low and high redshifts. With reference to Fig. 11, it can be seen that to shift the locus occupied by the passive *K*-bright galaxies at $z \simeq 1.4$ fully on to the local relation size–mass relation via major mergers would require a factor of $\simeq 5 - 6$ increase in stellar mass. This level of major merging is

completely inconsistent with *N*-body simulations, which suggest that the typical number of major mergers experienced in the redshift interval $0 < z < 1.5$ by galaxies with stellar masses $M_\star \geq 10^{11}\,\mathrm{M}_\odot$ is $\simeq$1 (e.g. Hopkins et al. 2010). Moreover, this level of stellar-mass growth is totally excluded by the constraints provided by the high-mass end of the local galaxy stellar-mass function. The latest derivation of the local galaxy stellar-mass function by Baldry et al. (2012) suggests that if the passive members of the *K*-bright sample were to grow in stellar mass by a factor of $\simeq$5, they would overshoot the observed number density of local galaxies with stellar masses $M_\star \geq 10^{11.5}\,\mathrm{M}_\odot$ by a factor of $\simeq$25.

Of course, it could reasonably be argued that the *K*-bright sample may suffer from significant progenitor bias and that the members of the passive sub-sample of the *K*-bright galaxies are not destined to fully populate the high-mass end of the local early-type size–mass relation. If, for example, they were only destined to populate the lower half of the size–mass relation, the amount of stellar-mass growth required would drop to a factor of $\simeq$2, seemingly making the major-merger scenario more plausible. However, if we again compare with the local galaxy stellar-mass function, we find that the effect of progenitor bias on the *K*-bright sample cannot be severe. Indeed, the results of Baldry et al. (2012) show that the number density of local galaxies with stellar masses $M_\star \geq 10^{11}\,\mathrm{M}_\odot$ is $n = (3.4 \pm 0.4) \times 10^{-4}\,\mathrm{Mpc}^{-3}$. Above this mass threshold, where the *K*-bright sample should be 100 per cent complete, the number density of *K*-bright galaxies is $n = (3.0 \pm 0.5) \times 10^{-4}\,\mathrm{Mpc}^{-3}$ ($\simeq$ 90 per cent of the local number density). Even if we restrict the comparison to only the passive members of the *K*-bright sample, they alone can account for $\simeq$68 per cent of the local number density of $M_\star \geq 10^{11}\,\mathrm{M}_\odot$ galaxies.

5.1.3 Major plus minor mergers

Given that there is strong evidence against major mergers being able to fully explain the observed size–mass evolution between $z \simeq 1.5$ and the present day, it is worth considering a toy model in which the additional mass growth is dominated by minor mergers, which can increase half-light radius in proportion to the square of the fractional increase in stellar mass (e.g. Naab et al. 2009). As can be seen from the top panel of Fig. 11, this mechanism potentially allows rapid growth in half-light radius, without requiring stellar-mass growth which violates the constraints provided by the local galaxy stellar-mass function.

In the bottom panel of Fig. 11, we illustrate the expected evolution of the passive members of the *K*-bright sample, based on a toy model which incorporates a mixture of major and minor merging activity. Specifically, the toy model assumes that, on average, each passive *K*-bright galaxy will undergo a single major merger between $z \simeq 1.4$ and the present day and that the likely mass ratio of this major merger will be 1:3. Additionally, the model also assumes that each galaxy undergoes a series of five minor mergers, each of which typically has a mass ratio of 1:10. In this scenario, the stellar mass of the galaxy increases by a factor of $\simeq$2 and the half-light radius increases by a factor of $\simeq$3.5. As can be seen in the bottom panel of Fig. 11, this toy scenario is at least capable of reconciling the observed size–mass relations for massive passive galaxies at $z \simeq 1.4$ and the present day, without requiring an unfeasible number of major (or minor) mergers. Moreover, in this toy model, the descendants of the passive *K*-bright galaxies do not violate the local galaxy stellar-mass function because they are predicted to contribute $\simeq$95 per cent of local number density of $M_\star \geq 10^{11}\,\mathrm{M}_\odot$ galaxies.

5.2 Passive discs and the quenching of star formation

As highlighted in Section 4.2, a substantial fraction of the passive members of the *K*-bright sample display a disc-like morphology. Indeed, of the 41 members of the *K*-bright sample which are classified as passive, according to our adopted sSFR $< 0.1\mathrm{Gyr}^{-1}$ criterion, nearly half (44 ± 12 per cent) have disc-like morphologies (i.e. $n < 2.5$). We note that this is consistent with the recent results of van der Wel et al. (2011), who estimated that 65 ± 15 per cent of passive galaxies at $z \simeq 2$ with stellar masses $M_\star \geq 6 \times 10^{10}\,\mathrm{M}_\odot$ have disc-dominated morphologies, based on *HST* imaging from the WFC3/IR Early Release Science programme.

In contrast, the results of a recent study by Bell et al. (2012), based on Sérsic profile fitting of the CANDELS WFC3/IR imaging in the UKIDSS UDS, suggest that at $z \simeq 1.5$ there are very few passive galaxies which do not have a prominent bulge component. Indeed, Bell et al. (2012) argue that a prominent bulge seems to be a necessary, but not sufficient, condition for quiescence. Although this would appear to contradict the results derived here, it is clearly possible that the passive disc-like galaxies identified in this study could also harbour a significant stellar bulge, which simply cannot be detected using ground-based imaging.

However, the high fraction of passive disc-like galaxies at $z \geq 1$ is confirmed by Bruce et al. (2012), based on a detailed disc/bulge decomposition analysis of the CANDELS WFC3/IR imaging in the UDS. Using a sample of $\simeq$200 galaxies with $M_\star \geq 10^{11}\,\mathrm{M}_\odot$ and photometric redshifts in the range $1.0 < z_{\mathrm{phot}} < 3.0$, Bruce et al. estimate that 25 ± 6 per cent of passive (sSFR$<0.1\mathrm{Gyr}^{-1}$) galaxies are disc dominated (i.e. $B/T < 0.5$), rising to 40 ± 7 per cent if they simply classify disc-dominated objects as having $n < 2.5$, based on a single Sérsic fit. It is therefore clear that a substantial fraction of massive, passive galaxies at $z > 1$ have a disc-like or even disc-dominated morphology.

It is likely that this simple observational fact contains crucial information about the evolutionary path followed by the progenitors of the massive galaxy population observed locally. As discussed in the previous section, the passive discs in the *K*-bright sample are expected to evolve into galaxies with $M_\star \geq 2 \times 10^{11}\,\mathrm{M}_\odot$, a mass regime which is dominated by ETGs in the local Universe. Consequently, massive disc galaxies at high redshift which have already been quenched are not a natural prediction of evolutionary models in which galaxy–galaxy mergers are responsible for quenching star formation *and* the morphological transformation from late type to early type.

However, the presence of massive, passive discs at $z \geq 1$ would appear to be in good qualitative agreement with recent hydrodynamical simulations of galaxy formation. Such simulations suggest that high-redshift star formation is dominated by filamentary inflows of cold gas ($T < 10^5$ K) until a critical redshift of $z_{\mathrm{crit}} \simeq 2$ at which point, at least for the most massive haloes, accretion of hot halo gas ($T > 10^5$ K) begins to dominate (e.g. Kereš et al. 2005). Moreover, at $z \leq 2$ gas is predicted to be shock heated to $T \simeq T_{\mathrm{vir}}$ in haloes with masses above a critical threshold ($M_{\mathrm{crit}} \simeq 10^{12}\,\mathrm{M}_\odot$), suppressing significant further accretion of gas and efficiently quenching star formation (e.g. Dekel & Bimboim 2006). A natural prediction of this model is therefore a significant population of massive ($M_\star \geq 10^{10.5}\,\mathrm{M}_\odot$, $M_{\mathrm{halo}} \geq 10^{12}\,\mathrm{M}_\odot$) quenched discs, which are then subsequently transformed into spheroids through a combination of both major and minor mergers at lower redshifts.

Finally, we note that this scenario is also in qualitative agreement with the phenomenological model of Peng et al. (2010), in which star formation quenching in the highest mass galaxies is independent

of environment and proportional to SFR. This scenario also predicts that morphological transformation and star formation quenching are separate physical processes and foresees star-forming discs rapidly quenching from the blue cloud on to the red sequence.

6 CONCLUSIONS

In this paper, we have presented the results of an analysis of the relationship between galaxy size, stellar mass and sSFR in a mass-complete ($M_\star \geq 6 \times 10^{11}\,\mathrm{M}_\odot$) sample of spectroscopically confirmed $1.3 \leq z \leq 1.5$ galaxies in the UKIDSS UDS field. Using stellar-mass measurements based on spectro-photometric SED fitting and galaxy size measurements based on two-dimensional modelling of the available UDS *K*-band imaging, we have investigated the evolution of massive galaxies on the size–mass plane as a function of sSFR, galaxy morphology and stellar population age. In addition, we have derived an alternative constraint on the average size evolution of massive galaxies since $z \simeq 1.4$ using dynamical-mass measurements for a small sub-sample of galaxies with reliable stellar-velocity-dispersion measurements. Finally, we have investigated evolutionary scenarios which can plausibly explain the observed size evolution without violating the constraints provided by both the latest *N*-body dark-matter simulations and current determinations of the local galaxy stellar-mass function. The main conclusions of this study can be summarized as follows.

(i) The location of massive galaxies ($M \geq 6 \times 10^{10}\,\mathrm{M}_\odot$) on the size–mass plane at $z \simeq 1.4$ is more closely correlated with sSFR than galaxy morphology.

(ii) Massive galaxies at $z \simeq 1.4$ which are passive (sSFR $\leq 0.1\ \mathrm{Gyr}^{-1}$) follow a tight size–mass relationship, which is identical in slope (and scatter) to that displayed by local ETGs in the SDSS. However, at a given stellar mass, passive galaxies at $z \simeq 1.4$ have half-light radii a factor of $f_\mathrm{g} = 2.43 \pm 0.20$ smaller than their low-redshift counterparts.

(iii) In contrast, massive star-forming galaxies at $z \simeq 1.4$ (sSFR $> 0.1\ \mathrm{Gyr}^{-1}$) lie closer to the size–mass relation of local late-type galaxies, but are still a factor of $f_\mathrm{g} = 1.61 \pm 0.17$ smaller than their low-redshift counterparts at a given stellar mass.

(iv) If the *K*-bright sample is split into early- and late-type morphologies using a Sérsic index threshold of $n = 2.5$, the corresponding growth factors are found to be $f_\mathrm{g} = 2.37 \pm 0.29$ and 2.15 ± 0.15 for early- and late-type galaxies, respectively. However, the ETG size–mass relation at $z \simeq 1.4$ displays a scatter which is noticeably larger than that associated with the passive galaxy size–mass relation. Moreover, the correspondence between passivity and early-type morphology (and active star formation and late-type morphology) in the *K*-bright sample is found to be weak.

(v) Using a small sub-sample of the *K*-bright galaxies with reliable stellar-velocity-dispersion measurements, an alternative constraint on the average size evolution between $z \simeq 1.4$ and the present day is obtained. The derived value of $f_\mathrm{g} = 2.33 \pm 0.32$ is entirely consistent with our primary determination based on stellar-mass measurements.

(vi) We demonstrate that a toy model which combines a single major merger with a sequence of five minor mergers can reproduce the observed size evolution of massive galaxies, without violating constraints imposed by the local galaxy stellar-mass function and the predictions of *N*-body simulations.

(vii) The significant fraction of passive galaxies with disc-like morphologies in the *K*-bright sample provides additional evidence that separate physical processes are responsible for the quenching of star formation and the subsequent morphological transformation in massive galaxies at $z \simeq 1.4$.

ACKNOWLEDGMENTS

The authors would like to acknowledge the efforts of the UKIRT staff for observing the UKIDSS UDS and Stéphane Charlot for providing the CB07 stellar population models. RJM would like to acknowledge the funding of the Royal Society via the award of a University Research Fellowship and the Leverhulme Trust via the award of a Philip Leverhulme research prize. MC acknowledges the award of an STFC Advanced Fellowship. JSD acknowledges the support of the Royal Society via a Wolfson Research Merit award, and also the support of the European Research Council via the award of an Advanced Grant. ECL would like to acknowledge financial support from the UK Science and Technology Facilities Council (STFC) and the Leverhulme Trust. FB acknowledges the support of the European Research Council. HJP, RC and EB acknowledge the award of an STFC PhD studentships. DGB and WGH acknowledge funding via the award of STFC PDRA grants. This work is based in part on data products from observations made with ESO Telescopes at the La Silla Paranal Observatory under ESO programme ID 179.A-2006 and on data products produced by the Cambridge Astronomy Survey Unit on behalf of the VIDEO consortium.

REFERENCES

Baldry I. K. et al., 2012, MNRAS, 421, 621
Barden M., Häußler B., Peng C. Y., McIntosh D. H., Guo Y., 2012, MNRAS, 422, 449
Bavouzet N., Dole H., Le Floc'h E., Caputi K. I., Lagache G., Kochanek C. S., 2008, A&A, 479, 83
Bell E. et al., 2012, ApJ, 753, 167
Bertin E., Arnouts S., 1996, A&AS, 117, 393
Bluck A. F. L., Conselice C. J., Buitrago F., Grutzbauch R., Hoyos C., Mortlock A., Bauer A. E., 2012, ApJ, 747, 34
Bruce V. A. et al., 2012, MNRAS, in press, arXiv:1206.4322
Bruzual G., Charlot S., 2003, MNRAS, 344, 1000 (BC01)
Buitrago F., Trujillo I., Concelice C. J., Bouwens R. J., Dickinson M., Yan H., 2008, ApJ, 687, L61
Calzetti D., Armus L., Bohlin R. C., Kinney A. L., Koornneef J., Storchi-Bergmann T., 2000, ApJ, 533, 682
Caputi K. I., Dunlop J. S., McLure R. J., Roche N. D., 2005, MNRAS, 361, 607
Chabrier G., 2003, PASP, 115, 763
Cimatti A. et al., 2002, A&A, 391, L1
Cimatti A. et al., 2008, A&A, 482, 21
Cimatti A., Nipoti C., Cassata, 2012, MNRAS, 422, L62
Cirasuolo M., McLure R. J., Dunlop J. S., Almaini O., Foucaud S., Simpson C., 2010, MNRAS, 401, 1166
Daddi E. et al., 2005, ApJ, 626, 680
Damjanov I. et al., 2009, ApJ, 695, 101
Dekel A., Bimboim Y., 2006, MNRAS, 368, 2
Elbaz D. et al., 2011, A&A, 533, A119
Fan L., Lapi A., De Zotti G., Danese L., 2008, ApJ, 689, L101
Furusawa H. et al., 2008, ApJS, 176, 1
Glazebrook K. et al., 2004, Nat, 430, 181
Grogin N. A. et al., 2011, ApJS, 197, 35
Hopkins P. F. et al., 2010, ApJ, 724, 915
Jarvis M. J. et al., MNRAS, in press (arXiv:1206.4263)
Johansson P. H., Naab T., Ostriker J. P., 2012, ApJ, 754, 115
Jorgensen I., Franx M., Kjaergaard P., 1996, MNRAS, 280, 167
Kauffmann G., Haehnelt M., 2000, MNRAS, 311, 576
Kennicutt R. C. Jr, 1998, ARA&A, 36, 189
Kereš D., Katz N., Weinberg D. H., Davé R., 2005, MNRAS, 363, 2
Koekemoer A. M. et al., 2011, ApJS, 197, 36

Kriek M. et al., 2010, ApJ, 722, L64
Lagache G., Dole H., Puget J.-L., 2003, MNRAS, 338, 555
Lawrence A. et al., 2007, MNRAS, 379, 1599
Le Borgne J. et al., 2003, A&A, 402, 433
Madau P., Pozzetti L., Dickinson M., 1998, ApJ, 498, 106
Mancini C. et al., 2010, MNRAS, 401, 933
Maraston C., 2005, MNRAS, 362, 799
Naab T., Johansson P. H., Ostriker J. P., 2009, ApJ, 669, L178
Newman A. B., Ellis R. S., Treu T., Bundy K., 2010, ApJ, 717, L103
Nipoti C., Treu T., Auger M. W., Bolton A. S., 2009, ApJ, 706, L86
Nipoti C., Treu T., Leauthaud A., Bundy K., Newman A. B., Auger M. W., 2012, MNRAS, 422, 1714
Oke J. B., Gunn J. E., 1983, ApJ, 266, 713
Oser L., Naab T., Ostriker J. P., Johansson P. H., 2012, ApJ, 744, 63
Peng C. Y., Ho L. C., Impey C. D., Rix H., 2002, AJ, 124, 266
Peng Y.-J. et al., 2010, ApJ, 721, 193
Ragone-Figueroa C., Granato G. L., 2011, MNRAS, 414, 3690
Saracco P., Longhetti M., Andreon S., 2009, MNRAS, 392, 718
Shen S., Mo H. J., White S. D. M., Blanton M. R., Kauffmann G., Voges W., Brinkmann J., Csabai I., 2003, MNRAS, 343, 978
Taylor E. N., Franx M., Glazebrook K., Brinchmann J., van der Wel A., van Dokkum P. G., 2010, ApJ, 720, 723
Toft S., Franx M., van Dokkum P., Forster-Schreiber N., Labbe I., Wuyts S., Marchesini D., 2009, ApJ, 705, 255
Trujillo I., Conselice C. J., Bundy K., Cooper M. C., Eisenhardt P., Ellis R. S., 2007, MNRAS, 382, 109
Trujillo I., Ferreras I., de La Rosa I. G., 2011, MNRAS, 415, 3903
Valentinuzzi T. et al., 2010, ApJ, 712, 226
van der Wel A., Holden B. P., Zirm A. W., Franx M., Rettura A., Illingworth G. D., Ford H. C., 2008, ApJ, 688, 48
van der Wel A. et al., 2011, ApJ, 730, 38
van Dokkum P. G., Kriek M., Franx M., 2009, Nat, 460, 717
van Dokkum P. G. et al.2010, ApJ, 709, 1018 (vD10)
Williams R. J., Quadri R. F., Franx M., van Dokkum P., Toft S., Kriek M., Labbe I., 2010, ApJ, 713, 738
Wuyts S. et al., 2011, ApJ, 742, 96
Zirm A. W. et al., 2007, ApJ, 656, 66

APPENDIX A: THE *K*-BRIGHT SAMPLE

In Table A1, we provide the basic observational properties and important derived quantities for the 81 objects in the *K*-bright sample.

Table A1. Basic measured and derived properties of the *K*-bright sample. The first three columns list the catalogue ID number and coordinates of each member of the sample. Columns 4 and 5 list the spectroscopic redshift (typical uncertainty $\delta z = 0.001$) and total *K*-band AB magnitude (uncertainty $\leq$5 per cent) for each object. Columns 6 and 7 list the derived half-light radii (circularized) and stellar masses along with their respective uncertainties. Columns 8–10 list the Sérsic index (typical uncertainty 30 per cent), sSFR and stellar population age (typical uncertainty 0.2 dex) for each object, respectively. The typical uncertainty on the derived sSFR values is dominated by the scatter associated with the adopted star formation calibrations and is a minimum of a factor of 2.

ID	RA(J2000)	Dec.(J2000)	z	$K_{\rm tot}$	r_c/kpc	$\log(M_\star/{\rm M}_\odot)$	n	sSFR/10^{-10} yr^{-1}	$\log_{10}$(age/yr)
34148	02:18:38.73	−05:11:41.7	1.280	20.5	$1.2^{+0.2}_{-0.2}$	$11.1^{+0.1}_{-0.1}$	3.0	0.22	9.3
30370	02:18:41.35	−05:13:58.2	1.289	21.0	$2.6^{+0.3}_{-0.3}$	$10.8^{+0.1}_{-0.2}$	0.9	14.5	9.6
28699	02:18:12.60	−05:15:01.2	1.290	21.3	$1.0^{+0.3}_{-0.3}$	$10.6^{+0.1}_{-0.1}$	3.9	18.4	9.6
69422	02:18:43.01	−04:51:17.0	1.296	20.3	$2.2^{+0.3}_{-0.4}$	$11.2^{+0.2}_{-0.1}$	6.1	0.18	9.5
80073	02:18:08.35	−04:45:01.6	1.299	20.3	$3.0^{+0.4}_{-0.3}$	$11.3^{+0.1}_{-0.1}$	3.6	0.02	9.5
76779	02:17:35.88	−04:46:57.1	1.303	21.5	$2.4^{+0.2}_{-0.2}$	$10.5^{+0.1}_{-0.1}$	1.1	1.65	8.9
65948	02:17:27.06	−04:53:18.6	1.305	20.7	$2.5^{+0.3}_{-0.3}$	$10.7^{+0.1}_{-0.1}$	0.8	23.0	9.3
63940	02:16:45.94	−04:54:28.3	1.311	21.5	$1.6^{+0.4}_{-0.2}$	$10.6^{+0.2}_{-0.1}$	2.8	0.08	9.4
53901	02:19:15.37	−05:00:12.8	1.313	19.9	$2.3^{+0.3}_{-0.2}$	$11.3^{+0.1}_{-0.1}$	3.5	1.34	9.5
32058	02:18:47.12	−05:12:56.6	1.315	21.1	$3.7^{+0.9}_{-0.9}$	$10.5^{+0.1}_{-0.1}$	4.5	2.63	9.2
58266	02:19:19.09	−04:57:47.0	1.316	20.1	$2.9^{+0.3}_{-0.3}$	$11.3^{+0.1}_{-0.1}$	1.1	14.1	9.6
42643	02:19:11.84	−05:06:43.8	1.319	19.9	$1.8^{+0.2}_{-0.2}$	$11.5^{+0.1}_{-0.1}$	3.6	0.22	9.7
79330	02:17:19.32	−04:45:22.1	1.320	21.2	$1.2^{+0.2}_{-0.2}$	$10.6^{+0.2}_{-0.1}$	1.4	32.5	8.8
29501	02:18:46.35	−05:14:28.0	1.320	21.1	$3.1^{+0.3}_{-0.3}$	$10.6^{+0.1}_{-0.1}$	1.0	1.48	9.1
46450	02:19:09.47	−05:04:37.0	1.320	20.8	$1.2^{+0.2}_{-0.1}$	$10.9^{+0.1}_{-0.1}$	1.6	0.20	9.3
77399	02:17:04.68	−04:46:31.5	1.321	20.1	$2.9^{+0.3}_{-0.3}$	$11.4^{+0.1}_{-0.1}$	2.2	0.19	9.7
46091	02:19:09.02	−05:04:48.5	1.321	20.3	$2.6^{+0.3}_{-0.3}$	$11.3^{+0.1}_{-0.1}$	3.9	0.04	9.6
50618	02:19:11.78	−05:02:09.2	1.321	20.5	$2.2^{+0.2}_{-0.2}$	$11.0^{+0.1}_{-0.1}$	2.5	1.51	9.5
65792	02:19:14.34	−04:53:23.2	1.322	21.1	$2.5^{+0.5}_{-0.3}$	$10.6^{+0.1}_{-0.1}$	3.3	27.4	9.2
79998	02:17:20.47	−04:45:06.6	1.323	21.0	$1.5^{+0.6}_{-0.3}$	$10.8^{+0.1}_{-0.1}$	5.3	0.61	9.5
50326	02:17:37.02	−05:02:21.7	1.325	21.1	$1.0^{+0.2}_{-0.2}$	$10.8^{+0.1}_{-0.1}$	4.6	0.03	9.6
77581	02:18:01.72	−04:46:27.2	1.326	21.1	$0.8^{+0.3}_{-0.3}$	$10.7^{+0.1}_{-0.1}$	2.7	0.20	9.5
53783	02:17:59.21	−05:00:20.4	1.329	21.4	$0.3^{+0.1}_{-0.1}$	$10.5^{+0.1}_{-0.1}$	4.1	2.20	9.2
73006	02:16:55.04	−04:49:10.4	1.331	20.8	$4.2^{+0.4}_{-0.4}$	$10.8^{+0.1}_{-0.1}$	1.0	13.8	9.0
60493	02:19:19.65	−04:56:25.0	1.332	19.8	$1.8^{+0.2}_{-0.2}$	$11.5^{+0.1}_{-0.1}$	6.2	0.28	9.5
75483	02:16:57.77	−04:47:42.6	1.372	20.3	$3.3^{+0.3}_{-0.3}$	$11.2^{+0.1}_{-0.2}$	2.5	0.33	9.6

Table A1 – *continued*

ID	RA(J2000)	Dec.(J2000)	z	$K_{\rm tot}$	r_c/kpc	$\log(M_\star/{\rm M}_\odot)$	n	sSFR/10^{-10} yr^{-1}	$\log_{10}$(age/yr)
78289	02:18:05.26	−04:46:02.9	1.380	21.4	$2.7^{+0.3}_{-0.3}$	$10.4^{+0.1}_{-0.1}$	1.4	14.5	9.3
73717	02:17:22.04	−04:48:46.3	1.380	21.3	$1.4^{+0.4}_{-0.3}$	$10.4^{+0.1}_{-0.1}$	1.4	44.7	9.3
42941	02:17:37.90	−05:06:37.2	1.394	21.1	$1.9^{+0.2}_{-0.2}$	$10.8^{+0.2}_{-0.1}$	2.0	1.25	9.2
77327	02:18:02.96	−04:46:36.4	1.399	20.6	$1.2^{+0.1}_{-0.1}$	$11.1^{+0.1}_{-0.1}$	3.5	0.07	9.5
79158	02:17:58.54	−04:45:29.9	1.399	20.0	$2.7^{+0.3}_{-0.3}$	$11.4^{+0.1}_{-0.2}$	1.5	0.35	9.5
49095	02:18:46.72	−05:03:03.7	1.401	20.8	$3.1^{+1.2}_{-0.5}$	$11.0^{+0.1}_{-0.1}$	5.8	1.30	9.5
79274	02:17:05.57	−04:45:30.3	1.401	21.3	$1.8^{+0.2}_{-0.2}$	$10.7^{+0.1}_{-0.1}$	1.8	3.36	9.6
45629	02:19:10.14	−05:05:07.6	1.401	21.4	$0.6^{+0.1}_{-0.2}$	$10.7^{+0.1}_{-0.1}$	5.6	0.20	9.4
61110	02:18:32.62	−04:56:04.1	1.402	20.6	$2.5^{+0.3}_{-0.3}$	$11.0^{+0.1}_{-0.1}$	2.1	0.73	9.5
56208	02:16:23.91	−04:58:59.0	1.402	20.7	$1.7^{+0.4}_{-0.2}$	$10.9^{+0.1}_{-0.1}$	4.9	1.09	9.3
54647	02:18:49.81	−04:59:51.2	1.404	21.1	$1.1^{+0.3}_{-0.4}$	$11.0^{+0.1}_{-0.1}$	8.0	0.50	9.6
63911	02:16:17.68	−04:54:26.8	1.405	20.5	$3.8^{+0.9}_{-0.4}$	$11.2^{+0.1}_{-0.1}$	3.5	0.04	9.5
57918	02:18:34.48	−04:58:00.1	1.407	20.8	$1.4^{+0.1}_{-0.1}$	$11.1^{+0.1}_{-0.2}$	1.6	0.02	9.6
56439	02:17:23.07	−04:58:47.8	1.408	19.8	$4.5^{+0.5}_{-0.5}$	$11.6^{+0.1}_{-0.1}$	2.0	0.37	9.6
45372	02:18:31.67	−05:05:14.8	1.408	20.4	$3.9^{+0.4}_{-0.4}$	$11.2^{+0.1}_{-0.2}$	2.3	0.54	9.5
44194	02:19:25.35	−05:05:52.1	1.408	20.2	$2.4^{+0.2}_{-0.2}$	$11.0^{+0.1}_{-0.1}$	1.6	2.98	9.2
54522	02:17:32.14	−04:59:55.0	1.411	21.0	$1.5^{+0.5}_{-0.2}$	$10.9^{+0.1}_{-0.1}$	3.7	0.05	9.3
59320	02:16:06.65	−04:57:06.8	1.409	20.0	$4.5^{+0.5}_{-0.5}$	$11.5^{+0.1}_{-0.2}$	2.2	0.36	9.4
32227	02:16:59.40	−05:12:50.7	1.410	20.9	$2.3^{+0.2}_{-0.2}$	$10.9^{+0.2}_{-0.1}$	1.0	19.9	9.1
49961	02:17:36.52	−05:02:33.0	1.411	20.5	$1.9^{+0.2}_{-0.2}$	$11.2^{+0.1}_{-0.1}$	2.9	0.48	9.5
63237	02:18:07.67	−04:54:51.4	1.412	21.0	$2.0^{+0.2}_{-0.2}$	$10.9^{+0.1}_{-0.1}$	2.1	0.23	9.5
46492	02:18:38.78	−05:04:34.2	1.414	20.5	$3.5^{+0.4}_{-0.4}$	$11.0^{+0.1}_{-0.1}$	1.2	15.0	9.4
52436	02:17:36.41	−05:01:07.1	1.421	20.5	$1.1^{+0.1}_{-0.1}$	$11.1^{+0.1}_{-0.1}$	2.6	21.5	9.3
63675	02:16:52.34	−04:54:37.3	1.429	21.1	$1.7^{+0.2}_{-0.2}$	$10.8^{+0.1}_{-0.1}$	1.1	20.2	9.0
81348	02:17:02.98	−04:44:21.3	1.435	21.5	$2.7^{+0.3}_{-0.3}$	$10.7^{+0.1}_{-0.1}$	1.2	9.40	9.6
29788	02:16:59.29	−05:14:19.9	1.435	21.4	$1.1^{+0.4}_{-0.4}$	$10.7^{+0.1}_{-0.1}$	1.9	0.63	9.3
62125	02:17:18.68	−04:55:26.7	1.441	19.8	$4.6^{+0.5}_{-0.5}$	$11.7^{+0.1}_{-0.2}$	5.6	0.02	9.6
53841	02:17:02.42	−05:00:18.0	1.444	20.8	$1.8^{+0.2}_{-0.2}$	$11.0^{+0.2}_{-0.1}$	1.8	0.22	9.2
46886	02:17:05.81	−05:04:23.1	1.451	21.3	$1.5^{+0.3}_{-0.3}$	$10.5^{+0.1}_{-0.1}$	1.3	0.93	9.1
78217	02:17:21.67	−04:46:03.4	1.456	20.7	$3.0^{+0.3}_{-0.3}$	$11.0^{+0.1}_{-0.1}$	3.5	1.00	9.5
48550	02:18:06.02	−05:03:26.1	1.456	20.9	$1.7^{+0.2}_{-0.2}$	$11.0^{+0.1}_{-0.2}$	1.3	7.68	9.4
47359	02:18:42.06	−05:03:58.5	1.456	20.3	$4.7^{+0.5}_{-0.5}$	$11.3^{+0.1}_{-0.1}$	2.5	0.08	9.5
73600	02:17:06.30	−04:48:50.4	1.458	21.2	$1.1^{+0.1}_{-0.4}$	$10.7^{+0.1}_{-0.1}$	0.9	0.06	9.3
58689	02:17:19.26	−04:57:34.1	1.459	21.3	$4.5^{+0.5}_{-1.8}$	$10.8^{+0.1}_{-0.1}$	8.0	1.15	9.2
64357	02:17:17.46	−04:54:13.5	1.460	21.3	$2.6^{+0.3}_{-0.3}$	$10.6^{+0.1}_{-0.1}$	1.0	19.7	9.4
79138	02:17:20.51	−04:45:32.4	1.461	20.9	$2.8^{+0.3}_{-1.1}$	$10.8^{+0.1}_{-0.1}$	2.5	23.4	9.2
78923	02:17:20.52	−04:45:41.3	1.462	20.8	$0.8^{+0.3}_{-0.2}$	$11.0^{+0.1}_{-0.1}$	6.0	0.14	9.6
44334	02:17:24.56	−05:05:48.6	1.467	20.1	$3.0^{+0.3}_{-0.3}$	$11.4^{+0.1}_{-0.1}$	2.5	5.09	9.5
62775	02:16:48.66	−04:55:06.2	1.467	21.1	$1.4^{+0.3}_{-0.4}$	$10.9^{+0.2}_{-0.1}$	1.1	5.73	9.2
66424	02:17:00.91	−04:53:03.4	1.467	20.9	$2.2^{+0.2}_{-0.2}$	$11.1^{+0.1}_{-0.2}$	1.5	0.80	9.5
71384	02:17:25.54	−04:50:07.9	1.477	20.0	$3.0^{+0.3}_{-0.3}$	$11.5^{+0.1}_{-0.1}$	3.5	0.26	9.6
72088	02:17:18.88	−04:49:45.7	1.477	21.4	$1.2^{+0.5}_{-0.4}$	$10.8^{+0.1}_{-0.2}$	2.1	2.04	9.5
72815	02:17:30.38	−04:49:18.2	1.477	21.3	$3.0^{+0.3}_{-0.3}$	$10.6^{+0.1}_{-0.1}$	0.5	32.4	8.9
70067	02:17:24.38	−04:50:55.5	1.478	21.1	$2.1^{+0.8}_{-0.5}$	$11.1^{+0.1}_{-0.1}$	5.9	0.27	9.5
60843	02:18:40.11	−04:56:14.5	1.478	21.4	$3.9^{+0.4}_{-0.4}$	$10.6^{+0.1}_{-0.2}$	0.8	35.3	9.2
53230	02:18:50.65	−05:00:36.3	1.478	20.6	$1.9^{+0.2}_{-0.5}$	$11.1^{+0.1}_{-0.1}$	8.0	5.13	9.4

Table A1 – *continued*

ID	RA(J2000)	Dec.(J2000)	z	$K_{\rm tot}$	r_c/kpc	$\log(M_\star/{\rm M}_\odot)$	n	sSFR/10^{-10} yr^{-1}	$\log_{10}$(age/yr)
56151	02:18:43.61	−04:59:01.1	1.483	20.8	$1.6^{+0.2}_{-0.2}$	$11.0^{+0.1}_{-0.1}$	1.7	0.44	9.4
52354	02:16:52.72	−05:01:11.0	1.483	21.4	$3.1^{+0.3}_{-0.3}$	$10.5^{+0.1}_{-0.1}$	0.9	42.5	9.0
29201	02:17:19.95	−05:14:40.5	1.485	21.4	$0.8^{+0.3}_{-0.3}$	$10.6^{+0.1}_{-0.1}$	3.5	0.75	9.1
48451	02:19:13.83	−05:03:25.4	1.485	20.3	$3.5^{+0.4}_{-0.4}$	$11.2^{+0.1}_{-0.1}$	2.2	11.0	9.3
43168	02:18:33.52	−05:06:28.1	1.491	21.0	$1.4^{+0.2}_{-0.6}$	$10.9^{+0.1}_{-0.2}$	7.7	1.84	9.4
47774	02:18:30.39	−05:03:50.1	1.497	21.1	$3.6^{+0.8}_{-0.4}$	$10.9^{+0.1}_{-0.1}$	2.5	2.93	9.4
50229	02:18:38.09	−05:02:24.3	1.498	21.0	$1.7^{+0.2}_{-0.2}$	$10.9^{+0.1}_{-0.1}$	1.5	0.16	9.5
54253	02:16:22.61	−05:00:01.8	1.502	20.4	$1.3^{+0.1}_{-0.1}$	$11.3^{+0.1}_{-0.1}$	4.1	0.04	9.5
61727	02:18:02.04	−04:55:43.6	1.505	20.7	$1.7^{+0.2}_{-0.2}$	$11.0^{+0.1}_{-0.2}$	2.4	0.02	9.4

This paper has been typeset from a TEX/LATEX file prepared by the author.